

A PPMAP analysis of the filamentary structures in Ophiuchus L1688 and L1689

A. D. P. Howard,^{1*} A. P. Whitworth,¹ M. J. Griffin,¹ K. A. Marsh² and M. W. L. Smith¹

¹*School of Physics and Astronomy, Cardiff University, 5 The Parade, Cardiff, CF24 3AA, UK*

²*IPAC, Caltech, 1200E California Boulevard, Pasadena, CA 91125, USA*

Accepted XXX. Received YYY; in original form ZZZ

ABSTRACT

We use the PPMAP (Point Process MAPPING) algorithm to re-analyse the *Herschel* and SCUBA-2 observations of the L1688 and L1689 sub-regions of the Ophiuchus molecular cloud. PPMAP delivers maps with high resolution (here 14'', corresponding to ~ 0.01 pc at ~ 140 pc), by using the observations at their native resolutions. PPMAP also delivers more accurate dust optical depths, by distinguishing dust of different types and at different temperatures. The filaments and prestellar cores almost all lie in regions with $N_{\text{H}_2} \gtrsim 7 \times 10^{21} \text{ cm}^{-2}$ (corresponding to $A_V \gtrsim 7$). The dust temperature, T , tends to be correlated with the dust opacity index, β , with low T and low β tend concentrated in the interiors of filaments. The one exception to this tendency is a section of filament in L1688 that falls – in projection – between the two B stars, S1 and HD147889; here T and β are relatively high, and there is compelling evidence that feedback from these two stars has heated and compressed the filament. Filament FWHMs are typically in the range 0.10 pc to 0.15 pc. Most filaments have line densities in the range $25 M_{\odot} \text{ pc}^{-1}$ to $65 M_{\odot} \text{ pc}^{-1}$. If their only support is thermal gas pressure, and the gas is at the canonical temperature of 10 K, the filaments are highly supercritical. However, there is some evidence from ammonia observations that the gas is significantly warmer than this, and we cannot rule out the possibility of additional support from turbulence and/or magnetic fields. On the basis of their spatial distribution, we argue that most of the starless cores are likely to disperse (rather than evolving to become prestellar).

Key words: keyword1 – keyword2 – keyword3

1 INTRODUCTION

In the past decade, far-infrared and sub-millimetre dust observations have greatly enhanced our understanding of the star formation process within the Milky Way. Extensive surveys conducted with telescopes such as *Herschel*¹ and the JCMT have helped to disentangle the complicated nature of molecular clouds, revealing widespread networks of dense filaments (André et al. 2010; Arzoumanian et al. 2011; Hacar et al. 2013; Könyves et al. 2015; Arzoumanian et al. 2019; Ladjelate et al. 2020), and linking them to the earliest stages of pre- and protostellar core formation (André et al. 2014; Pattle et al. 2015; Marsh et al. 2016; Ladjelate et al. 2020).

The Ophiuchus molecular cloud complex is a nearby (~ 140 pc, Mamajek 2008), well studied region of star formation associated with the Gould Belt (Wilking & Lada 1983; Nutter et al. 2006; Pattle et al. 2015; Soler 2019; Ladjelate et al. 2020). The complex can be broken into a number of visually distinct sub-regions, the two most massive of which are L1688 and L1689. The Sco OB2 association, which is just 11 ± 3 pc away (Mamajek 2008), is thought to have a strong influence on the region, driving elongated streamers away from the dense heart of the complex (Vrba 1977; Loren 1989). The

L1688 sub-region, which is closer to Sco OB2, appears to be forming stars more actively than L1689 (Nutter et al. 2006).

Despite the early identification of filamentary structures associated with the Ophiuchus complex, most studies have focused on the pre- and protostellar cores within L1688 and L1689 (e.g. Nutter et al. 2006; Pattle et al. 2015), due to the limitations associated with observing extended structures with ground-based telescopes. Recent studies have analysed the filament networks, but have tended to do so in general terms, presenting the average properties of the entire ensemble of structures (e.g. Arzoumanian et al. 2019; Ladjelate et al. 2020).

In this paper, we re-analyse *Herschel* and SCUBA-2 observations of the L1688 and L1689 sub-regions of the Ophiuchus cloud complex, using the Bayesian PPMAP algorithm (Marsh et al. 2015). Section 2 describes the observations of the Ophiuchus complex. Section 3 lists the approximations that are made, and derives the factor for converting dust optical depths into surface densities (in $M_{\odot} \text{ pc}^{-2}$) and column-densities of molecular hydrogen (in cm^{-2}). Section 4 outlines the operation of the PPMAP algorithm. Section 5 presents the basic PPMAP data products for L1688 and L1689, and discusses the wide scale variations in dust properties across the two sub-regions. Section 6 investigates and compares the mass distributions and core formation efficiencies in L1688 and L1689. Section 7 gives a detailed analysis of the network of filaments across Ophiuchus, and examines

* E-mail: Alexander.Howard@astro.cf.ac.uk (CU)

¹ *Herschel* is an ESA space observatory with science instruments provided by European-led Principal Investigator consortia and with important participation from NASA.

the impact of feedback from nearby B stars on the largest filamentary structure. Section 8 summarises our main conclusions.

2 OBSERVATIONS OF OPHIUCHUS

2.1 Herschel observations

The *Herschel* observations of the Ophiuchus molecular cloud were taken as part of the *Herschel Gould Belt Survey* (HGBS)². They consist of 70 μ m and 160 μ m data from PACS (Poglitsch et al. 2010), and 250 μ m, 350 μ m and 500 μ m data from SPIRE (Griffin et al. 2010). The scans were taken in the fast scan (60'' s⁻¹) PACS/SPIRE parallel mode, and comprise a single pair of nominal and orthogonal scans, both taken on 25 September 2010. The *Herschel* Observation IDs for these scans are 1342205093 and 1342205094, respectively.

The observations were reduced using the HIPE User Release v15.0.1. PACS maps were produced using a modified version of the JScanam task, whilst SPIRE maps were produced with the mosaïc script operating on Level 2 data products. We determined the Zero-Point Offsets for the PACS maps through comparison with *Planck* and IRAS observations of the same region (cf. Bernard et al. 2010). The adopted offsets were -8.4 MJy sr⁻¹ and 243.5 MJy sr⁻¹ for the 70 μ m and 160 μ m bands, respectively.³ The SPIRE Zero-Point Offsets were applied automatically as part of the reduction process.

The FWHMs of the circular beam profiles used by PPMAP are 8.5'', 13.5'', 18.2'', 24.9'', and 36.3'', for – respectively – the 70 μ m, 160 μ m, 250 μ m, 350 μ m, and 500 μ m wavebands (Exter 2017; Valtchanov 2017). In reality, the PACS beams are distorted by the fast scan PACS/SPIRE parallel mode, producing effective non-circular beamsizes of $\sim 6'' \times 12''$ for the 70 μ m waveband, and $\sim 12'' \times 16''$ for the 160 μ m waveband, but this is not taken into account in the standard PPMAP procedure.

2.2 SCUBA-2 observations

As in Howard et al. (2019), we use SCUBA-2 (Holland et al. 2013) 850 μ m observations to supplement the *Herschel* data. These observations were taken as part of the JCMT Gould Belt Survey (Ward-Thompson et al. 2007), and have an angular resolution of 14.6''. The observations consist of 30' diameter circular regions generated using the PONG1800 mapping mode (Chapin et al. 2013), and were mosaicked together as described in Pattle et al. (2015).

A 10' high-pass filter was used in the reduction of the SCUBA-2 observations to remove the effects of atmospheric and instrumental noise. This has the effect of removing emission from structure larger than 10' in extent. We restore the larger spatial scales by combining the SCUBA-2 observations with the 850 μ m *Planck* map of the region, using a customised feathering technique in python. The feathering uses the same core routine as the CASA FEATHER task⁴, where both maps are first converted to the Fourier-plane, and then the low-resolution image is scaled by the ratio of the beam volumes.

² <http://www.herschel.fr/cea/gouldbelt/en/>

³ These are different from the offsets used by Ladjelate et al. (2020) (their Table 1), possibly because of the different smoothing they apply and/or differences in the reduction procedure used on the PACS data. If we were to adopt the Ladjelate et al. (2020) offsets, we would obtain lower dust temperatures and therefore larger dust optical depths. However, this would be partially compensated by the fact that PPMAP does not overestimate the contribution from warmer than average dust.

⁴ <https://casa.nrao.edu/casadocs/casa-5.4.1/image-combination/feather#cit1>

The Fourier-transformed high-resolution image is then weighted by $(1 - \text{FT}_{\text{beam}})$ where FT_{beam} is the Fourier-transform of the low-resolution image beam, and in this code we assume the beams are Gaussian. Finally the high and low-resolution datasets are added and inverse Fourier-transformed to produce the combined image. Tests of this script on extra-galactic targets show that the recovered flux-densities are accurate to $\sim 10\%$. Moreover, the maps presented here are likely to be better than this, since the SCUBA-2 maps preserve emission scales up to 10' scales, whereas extragalactic maps typically use a harsher filter ($\sim 6'$). The algorithm, and tests of its fidelity when applied to SCUBA-2 data, will be submitted for publication shortly (Smith et al., in prep.).

Fig. 1 shows the *Herschel* and SCUBA-2 observations used in this paper, and the boundaries of the sub-regions encompassing the L1688 and L1689 objects (see Lynds 1962). As the boundaries of L1688 and L1689 are not well defined, we chose the coverage of these sub-regions based on the extent of the SCUBA-2 observations, seeking to exclude areas that have not been observed, while at the same time enclosing the brightest regions. The L1688 sub-region has an angular size of 1.2° by 0.8° centred on RA = 246.75° and Dec = -24.47°. The L1689 region encompasses an area of 1.0° by 1.0° centred on RA = 248.25° and Dec = -24.67°.

3 APPROXIMATIONS

3.1 Opacity Law

We follow the convention of approximating the long-wavelength variation of the mass opacity, κ_{λ} , with wavelength, λ , as a power law with opacity index, β :

$$\kappa_{\lambda} = \kappa_0 \left(\frac{\lambda}{\lambda_0} \right)^{-\beta}. \quad (1)$$

Here κ_0 is the mass opacity (per unit mass of dust and gas) at the reference wavelength, for which we adopt $\lambda_0 = 300 \mu\text{m}$.

3.2 Conversion factors

The optical depth, τ_0 , at the reference wavelength, λ_0 , is related to the surface-density of gas and dust, Σ , by $\tau_0 = \Sigma\kappa_0$, and hence

$$\Sigma = \frac{\tau_0}{\kappa_0}. \quad (2)$$

If the fractional abundance of hydrogen by mass is X_{H} , and the fraction of hydrogen that is molecular is X_{H_2} , the column-density of molecular hydrogen is

$$N_{\text{H}_2} = \frac{X_{\text{H}} X_{\text{H}_2} \Sigma}{2m_{\text{H}}} = \frac{X_{\text{H}} X_{\text{H}_2} \tau_0}{2m_{\text{H}} \kappa_0}, \quad (3)$$

where $m_{\text{H}} = 1.67 \times 10^{-24}$ g is the mass of an hydrogen atom.

However, the fundamental quantity estimated by PPMAP from the analysis of *Herschel* and SCUBA-2 maps is the dust optical-depth, τ_0 , at the reference wavelength, λ_0 . Converting τ_0 into Σ (Eq. 2) or N_{H_2} (Eq. 3) requires the specification of κ_0 , X_{H} and X_{H_2} , all of which are uncertain and all of which are expected to vary with position – especially κ_0 and X_{H_2} . Parenthetically these parameters also have no bearing on the workings of PPMAP. For those who wish to convert τ_0 into Σ , we suggest $\kappa_0 = 0.10 \text{ cm}^2 \text{ g}^{-1} = 2.1 \times 10^{-5} \text{ pc}^2 \text{ M}_{\odot}^{-1}$, which is consistent with the opacity coefficient proposed by Hildebrand (1983) for a fractional dust abundance of $Z_{\text{D}} = 0.01$, and gives

$$\Sigma = \left[4.8 \times 10^4 \text{ M}_{\odot} \text{ pc}^{-2} \right] \tau_0. \quad (4)$$

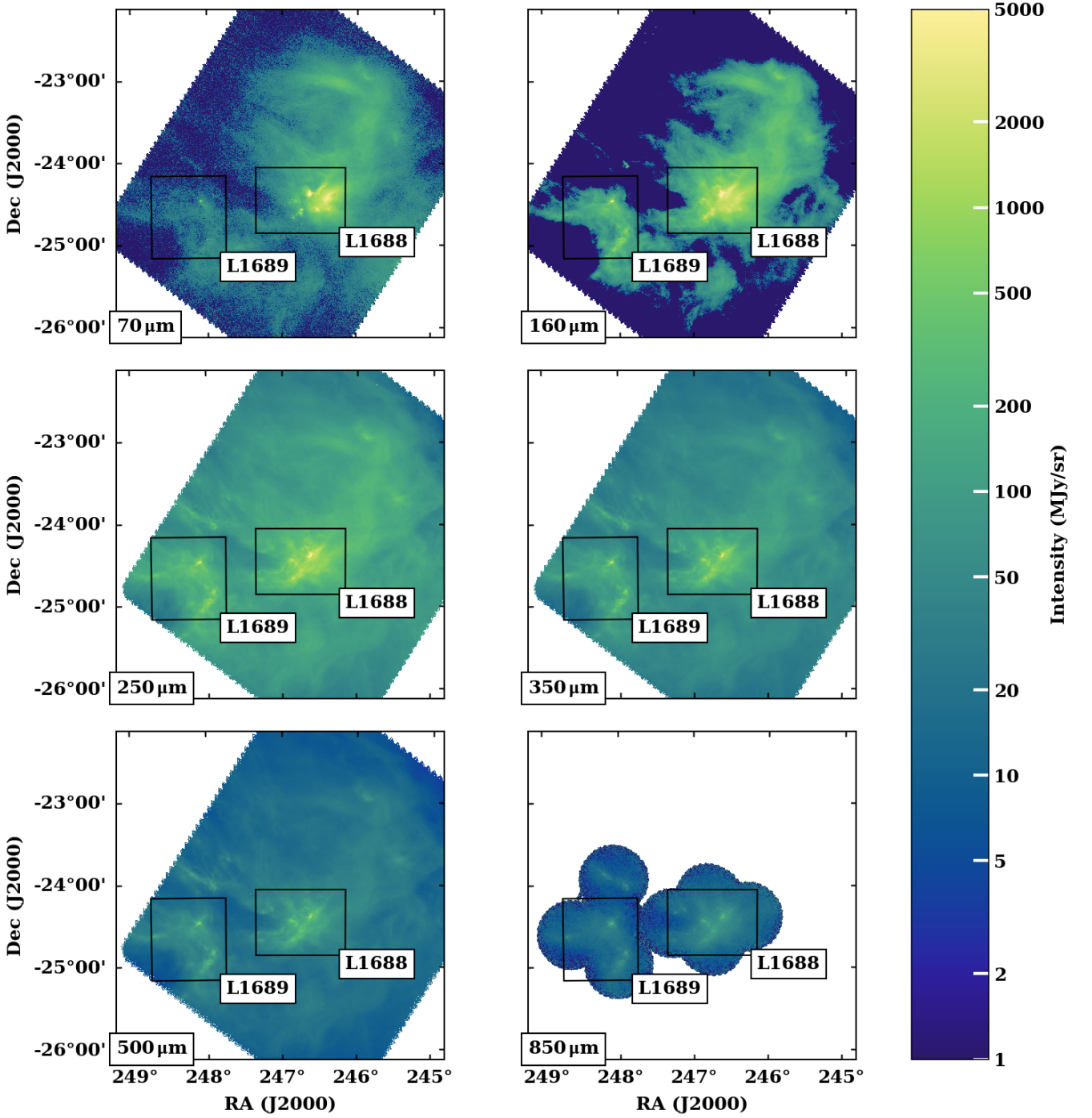


Figure 1. Intensity maps of Ophiuchus in the *Herschel* bands at 70 μm , 160 μm , 250 μm , 350 μm and 500 μm , plus the SCUBA-2 band at 850 μm . The black rectangles delineate the L1688 and L1689 sub-regions.

For those who wish to convert τ_0 into N_{H_2} , we suggest $X_{\text{H}} = 0.70$ and $X_{\text{H}_2} \simeq 1.00$, whence

$$N_{\text{H}_2} = \left[2.1 \times 10^{24} \text{ cm}^{-2} \right] \tau_0. \quad (5)$$

The total mass on the line of sight through a pixel of angular size

$\Delta\Omega_{\text{pixel}}$ is

$$\begin{aligned} \Delta M_{\text{pixel}} &= \Sigma (\Delta\Omega_{\text{pixel}}/\text{steradian}) D^2 \\ &= [0.011 M_{\odot}] \tau_0 \left(\frac{\Delta\Omega_{\text{pixel}}}{\text{arcsec}^2} \right) \left(\frac{D}{100 \text{ pc}} \right)^2, \end{aligned} \quad (6)$$

where D is the distance to the observed region and τ_0 is the optical depth through the pixel, at the reference wavelength.

3.3 Caveats

The factors in square brackets in Eqs. (4) through (6) are *not* accurate to two significant figures. Furthermore, when we derive variations in the opacity index, β , we should be mindful that these variations are probably due to grain growth/erosion and/or coagulation/fragmentation. Such changes are likely to be accompanied by correlated changes in the dust absorption opacity at the reference wavelength, κ_0 . The magnitudes of these changes are not currently known, and even their sense is not established with total certainty. This uncertainty does not affect the variations in β which we detect, but it does affect the amount of mass (Σ) or molecular hydrogen (N_{H_2}) associated with the different types of dust. Thus, when we refer to the line-of-sight mean dust opacity index, $\bar{\beta}$ (e.g. Eq. 15), or the line-of-sight mean temperature, \bar{T} (e.g. Eq. 14), we should be mindful that these are optical-depth weighted means, and not – strictly speaking – mass-weighted means. In contrast, the means returned by conventional modified black body fitting routines are flux-weighted means.

4 THE PPMAP ALGORITHM

In the standard Modified BlackBody (MBB) fitting procedure the observations in the different wavebands are smoothed to the coarsest resolution (here the 36.3'' of the *Herschel* 500 μm waveband), thereby discarding a large amount of information. The intensity in each pixel is then fitted with a single average optical depth, $\bar{\tau}_0$, and a single average dust temperature, \bar{T} (i.e. flux-weighted averages along the line of sight through the pixel),

$$I_\lambda = \bar{\tau}_0 \left(\frac{\lambda}{\lambda_0} \right)^{-\beta} B_\lambda(\bar{T}), \quad (7)$$

with $\beta=2$ (e.g. Hildebrand 1983; André et al. 2010; Schneider et al. 2012; Könyves et al. 2015; Ladjelate et al. 2020). In principle, the emissivity index, β , can also be treated as a free parameter, but in practice this endeavour is compromised by the fact that lower values of β are very hard to distinguish from higher values of T , and vice versa (Shetty et al. 2009a,b), particularly if there are no observations at long wavelengths well above the peak of the SED. The resolution can be improved by a factor of two by bootstrapping off the *Herschel* 250 μm observations (Palmeirim et al. 2013), but this is only reliable if there is a low temperature variance along the line of sight. The maps of Ophiuchus presented in Ladjelate with 18'' resolution are obtained using the Palmeirim bootstrapping procedure

In contrast to standard MBB fitting procedure, PPMAP (Point-ProcessMAPping; Marsh et al. 2015) does not degrade the set of input observations to the coarsest common resolution. Instead, it utilises high-fidelity beam profiles for each of the observing bands, and thereby retains some of the extra information contained within the observations at their native resolutions.

The PPMAP data products derived here for the Ophiuchus sub-regions have 14'' angular resolution in order to make the best use of the information provided by the PACS 70 μm observations (with a distorted minimum resolution of 12'') and the SCUBA-2 850 μm observations (with a resolution of 14.6''). The average distance to the Ophiuchus sub-regions is $D \approx 140$ pc (Mamajek 2008). Therefore, the 14'' resolution corresponds to ~ 0.01 pc (or ~ 2000 AU). In principle, PPMAP can deliver maps at the finest observed resolution (i.e. the 8.5'' of the 70 μm waveband, as demonstrated in the analysis of M31 presented in Whitworth et al. (2019)), but this requires higher signal-to-noise than we have for Ophiuchus.

PPMAP presumes that the total emission observed in each pixel is likely to involve contributions from different populations of dust along the line of sight, with different absorption properties and different dust temperatures. The differing dust absorption properties are represented by different discrete values of β , labelled β_k . In this work we use three linearly spaced values, $\beta_1 = 1.0$, $\beta_2 = 1.5$ and $\beta_3 = 2.0$.⁵ While each value of β_k is a discrete, delta function, the values are intended to encompass all opacity indices within a small interval centred on β_k ; for example, $\beta_1 = 1.0$ represents the opacity index range from 0.75 to 1.25.

Similarly, the different dust temperatures are represented by a series discrete values, labelled T_ℓ . Here we use twelve logarithmically spaced values, $T_1 = 7.0$ K, $T_2 = 8.4$ K, $T_3 = 10.0$ K, $T_4 = 12.0$ K, $T_5 = 14.3$ K, $T_6 = 17.1$ K, $T_7 = 20.5$ K, $T_8 = 24.5$ K, $T_9 = 29.2$ K, $T_{10} = 35.0$ K, $T_{11} = 41.8$ K, and $T_{12} = 50.0$ K. Again, T_ℓ is intended to represent a small range of dust temperature; for example, $T_1 = 7.0$ K represents the dust temperature range from 6.4 K to 7.7 K, and similarly for the other T_ℓ values.

The PPMAP algorithm assumes that the dust emission is optically thin. Therefore optically thick regions, such as protostellar cores (Ossenkopf & Henning 1994), are poorly fit by the algorithm. In cases where the emission from such cores dominates over the cloud emission, they must be masked out before the observations are analysed. Initial tests have demonstrated that in Ophiuchus, masking is only necessary for the L1689-IRS6 Class I protostar (Greene et al. 1994) and the 16293-2422 binary/multiple Class 0 protostellar system (Mundy et al. 1992). A 40'' diameter circular mask has been applied to each of the observation bands at the centroid positions of these two sources. The masks appear as small white circles on the PPMAP maps of the L1689 sub-region. There are other protostellar cores that are optically thick (for example at RA = 246° 48, Dec = -24° 19.5' on Fig. 4), but their effect is sufficiently small and local that we can reasonably ignore them.

PPMAP assumes that the observed intensity in each pixel on the sky, (i, j) , can be approximated by

$$I_\lambda = \sum_{k=1}^{k=3} \sum_{\ell=1}^{\ell=12} \left\{ \Delta^2 \tau_{0:k\ell} \left(\frac{\lambda}{\lambda_0} \right)^{-\beta_k} B_\lambda(T_\ell) \right\}, \quad (8)$$

where $\Delta^2 \tau_{0:k\ell}$ is the contribution to the total optical depth, τ_0 , at the reference wavelength, $\lambda_0 = 300$ μm , from dust along the line of sight with $\beta \sim \beta_k$ and $T \sim T_\ell$.

PPMAP constructs a model of the distribution of dust optical depth based on these assumptions. Therefore the raw data products from PPMAP are four-dimensional data-hypercubes, with two dimensions representing position on the sky, (x_i, y_j) , one dimension representing the opacity index, β_k , and one dimension representing the dust temperature, T_ℓ . Two data-hypercubes are produced, one giving the expectation values for $\Delta^2 \tau_{0:k\ell}$, and the other giving the corresponding uncertainties $\Delta^2 \sigma_{0:k\ell}$.

The data-hypercubes are produced using a Bayesian point process algorithm. Initially, the algorithm populates the optical depth data-hypercube with a uniform array of very small optical-depth quanta, $\delta\tau_{300\mu\text{m}}$. The emission that such a distribution would produce in each of the observation wavebands is compared with the true observations, taking into account the effects of the instrument beam profiles and colour corrections, and initially assuming an extremely

⁵ In exploratory work we invoked a fourth discrete β value, $\beta_4 = 2.5$, but the contribution to the optical depths from this dust was negligible, and therefore we dropped it from consideration.

high – artificially inflated – level of noise. The distribution of optical-depth quanta is then adjusted to improve the fit between the predicted intensities and the observed intensities. Due to the initially high level of artificial noise, the fit seems quite good and so the adjustments are small, i.e. in the linear regime. The comparison and adjustment process is performed iteratively, and the artificial noise is reduced with each iteration until it is completely removed and the predicted intensities (i.e. Eq. 8) closely match the observed intensities. Details of the algorithm are given in Marsh et al. (2015), along with a range of tests on synthetic data. The algorithm invokes a tight, Gaussian prior on β , in order to mitigate the (β, T) degeneracy (i.e. the fact that, for data sets with limited wavelength range, low β can be mimicked by high T , and vice versa; Shetty et al. 2009a,b). For Ophiuchus, we adopt a prior with mean $\mu_\beta = 2.0$ and standard deviation $\sigma_\beta = 0.25$. The tight prior on β ensures that the algorithm only deviates from the canonical value of $\beta = 2.0$ when the data really require this. A flat prior is used for $\log(T)$.

5 PPMAP DATA PRODUCTS

5.1 Basic data products

The four dimensional data-hypercubes produced by the PPMAP algorithm are hard to visualise. However, given the expectation values, $\Delta^2\tau_{0:k\ell}$, we can marginalise out one of the line of sight dimensions, β_k or T_ℓ , to produce a three dimensional data-cube. These data-cubes are analogous to position-position-velocity data-cubes derived from spectral line analysis, but with the velocity dimension replaced with either opacity index β or dust temperature T , and with the integrated intensity replaced with optical depth. The results can then be displayed as a sequence of 2D images.

By marginalising out the β dimension, we obtain

$$\Delta\tau_{0:\ell} = \sum_{k=1}^{k=3} \left\{ \Delta^2\tau_{0:k\ell} \right\}, \quad (9)$$

where $\Delta\tau_{0:\ell}$ is the contribution to the total line of sight opacity from dust at temperature T_ℓ .

Similarly, by marginalising out the T dimension, we obtain

$$\Delta\tau_{0:k} = \sum_{\ell=1}^{\ell=12} \left\{ \Delta^2\tau_{0:k\ell} \right\}, \quad (10)$$

where $\Delta\tau_{0:k}$ is the contribution to the total line of sight opacity from dust with opacity index β_k .

A two dimensional map of the expectation value for the total optical depth is obtained by marginalising out both β and T ,

$$\tau_0 = \sum_{\ell=1}^{\ell=12} \sum_{k=1}^{k=3} \left\{ \Delta^2\tau_{0:k\ell} \right\}. \quad (11)$$

The corresponding 2D map of the uncertainty on the expectation value is obtained by summing the individual contributions from β and T in quadrature

$$\sigma_0 = \left(\sum_{\ell=1}^{\ell=12} \sum_{k=1}^{k=3} \left\{ \left(\Delta^2\sigma_{0:k\ell} \right)^2 \right\} \right)^{1/2}. \quad (12)$$

By combining Eqs. (11) and (12), we produce a map of the Point Process Statistical Degeneracy,

$$\text{PPSD} = \tau_0 / \sigma_0. \quad (13)$$

PPSD is a measure of how statistically significant the PPMAP optical

depth estimates are, on a pixel-by-pixel basis, and is analogous to a signal-to-noise ratio.

Additionally, we can obtain maps of the mean dust temperature,

$$\bar{T} = \frac{1}{\tau_0} \sum_{\ell=1}^{\ell=12} \left\{ T_\ell \Delta\tau_{0:\ell} \right\}, \quad (14)$$

and the mean dust opacity index,

$$\bar{\beta} = \frac{1}{\tau_0} \sum_{k=1}^{k=3} \left\{ \beta_k \Delta\tau_{0:k} \right\}, \quad (15)$$

along each line of sight.

As discussed in §3.2, while PPMAP estimates dust opacity, we present our results in terms of the surface density of gas and dust, Σ , using Eq. (4). We note, however, that the observations, and thus the PPMAP models, trace dust rather than directly tracing gas.

Note that on Figs. 1 through 13, the scales of the colour bars for intensity, surface-density and dust temperature are logarithmic. This means that, in order to draw out the important features, the range of values represented must have a finite minimum and a finite maximum, and cannot extend down to zero. On the plots, but not in the analysis, positive values that fall below this minimum value are increased to the minimum. In pixels where there is no value (or in the case of fluxes, especially those from near the edges of the SCUBA2 pointings, negative values) these values are set to zero and the pixels are white.

5.2 L1688

Fig. 2 shows the temperature slices for the L1688 sub-region of Ophiuchus at nine contiguous temperatures ($T_3 = 10.0$ K, $T_4 = 12.0$ K, $T_5 = 14.3$ K, $T_6 = 17.1$ K, $T_7 = 20.5$ K, $T_8 = 24.5$ K, $T_9 = 29.2$ K, $T_{10} = 35.0$ K, $T_{11} = 41.8$ K). On large scales, there is a temperature gradient, from colder material ($\lesssim 14$ K) towards the east of the sub-region, to warmer material ($\gtrsim 17$ K) through the centre and towards the western edge. Several filamentary structures can be seen throughout the sub-region. While these structures subscribe to the large scale temperature gradient, it is also generally true that any single structure which dominates over its local background in lower-temperatures slices appears to fade relative to that background as we progress to higher temperatures, until only the local background is present. This indicates that the dense, filamentary structures are typically somewhat colder than their surroundings. Two regions of diffuse, hot ($\gtrsim 29$ K) dust surround the pre-main sequence objects S1 and HD147889 (red star markers), suggesting significant local heating by these young B stars.

Fig. 3 shows the opacity-index slices for the L1688 sub-region for all three discrete values of β . The $\beta_1 = 1.0$ slice is dominated by the structures associated with material in the coldest (10.0 K) slice of Fig. 2. Warmer structures, and the diffuse background environment, are better traced by material with higher opacity index $\beta \gtrsim 1.5$. This suggests that there is a change in the optical properties of dust in colder environments, similar to the trend found by Howard et al. (2019) in the Taurus molecular cloud.

Fig. 4 shows the estimated total surface density, Σ , derived from Eqs. (4) and (11). The filamentary structures observed in Fig. 2 are clearly visible in this map of total column density, and can also be cross referenced with the dense clumps (Rho Oph A through Rho Oph F) identified by Loren et al. (1990) from observations of DCO⁺. The approximate locations of these clumps are shown by the letter identifiers on Fig. 4. The low density regions surrounding S1 and

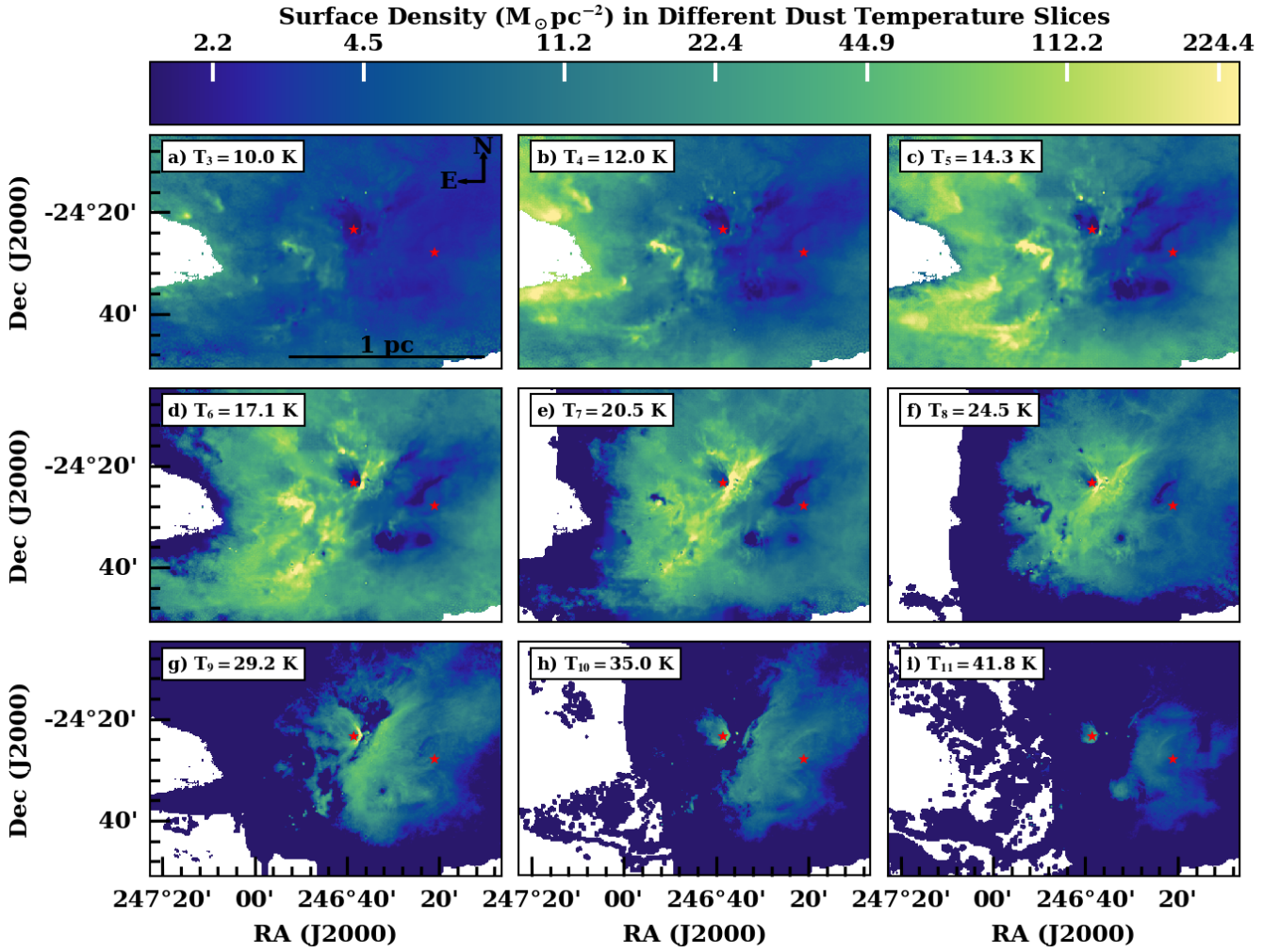


Figure 2. Nine contiguous PPMAP temperature slices for the L1688 sub-region, showing the estimated surface density, Σ , as traced by dust having temperature represented by the value marked in the top left. The red stars indicate the positions of the S1 and HD147889 pre-main sequence B stars.

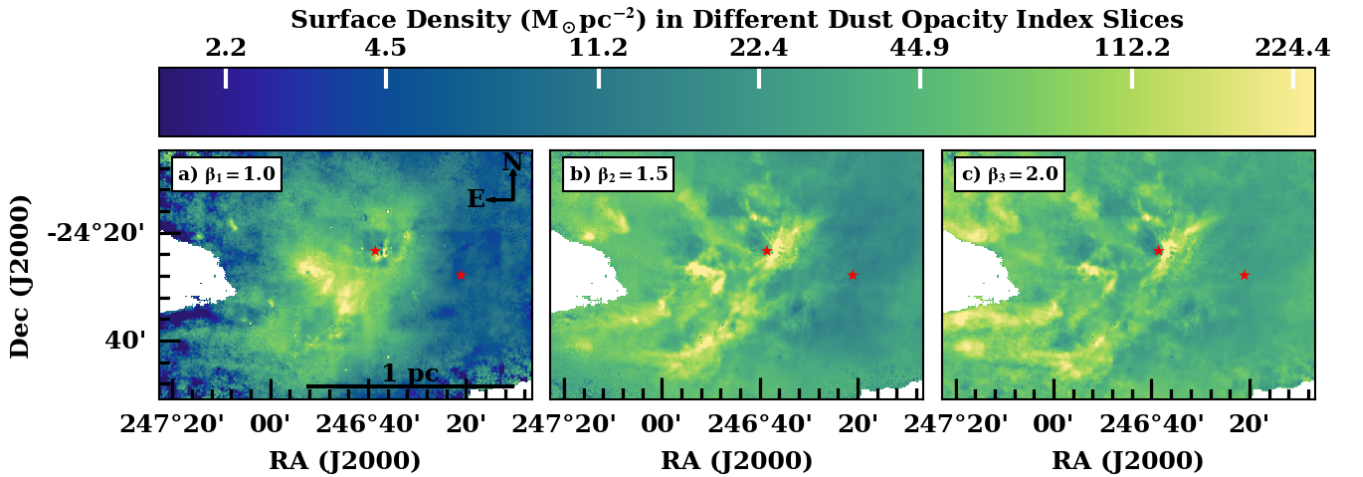


Figure 3. Three contiguous PPMAP opacity-index slices for the L1688 sub-region, showing the estimated surface density, Σ , as traced by dust with β close to the value marked in the top left. The red stars indicate the positions of the S1 and HD147889 pre-main sequence B stars.

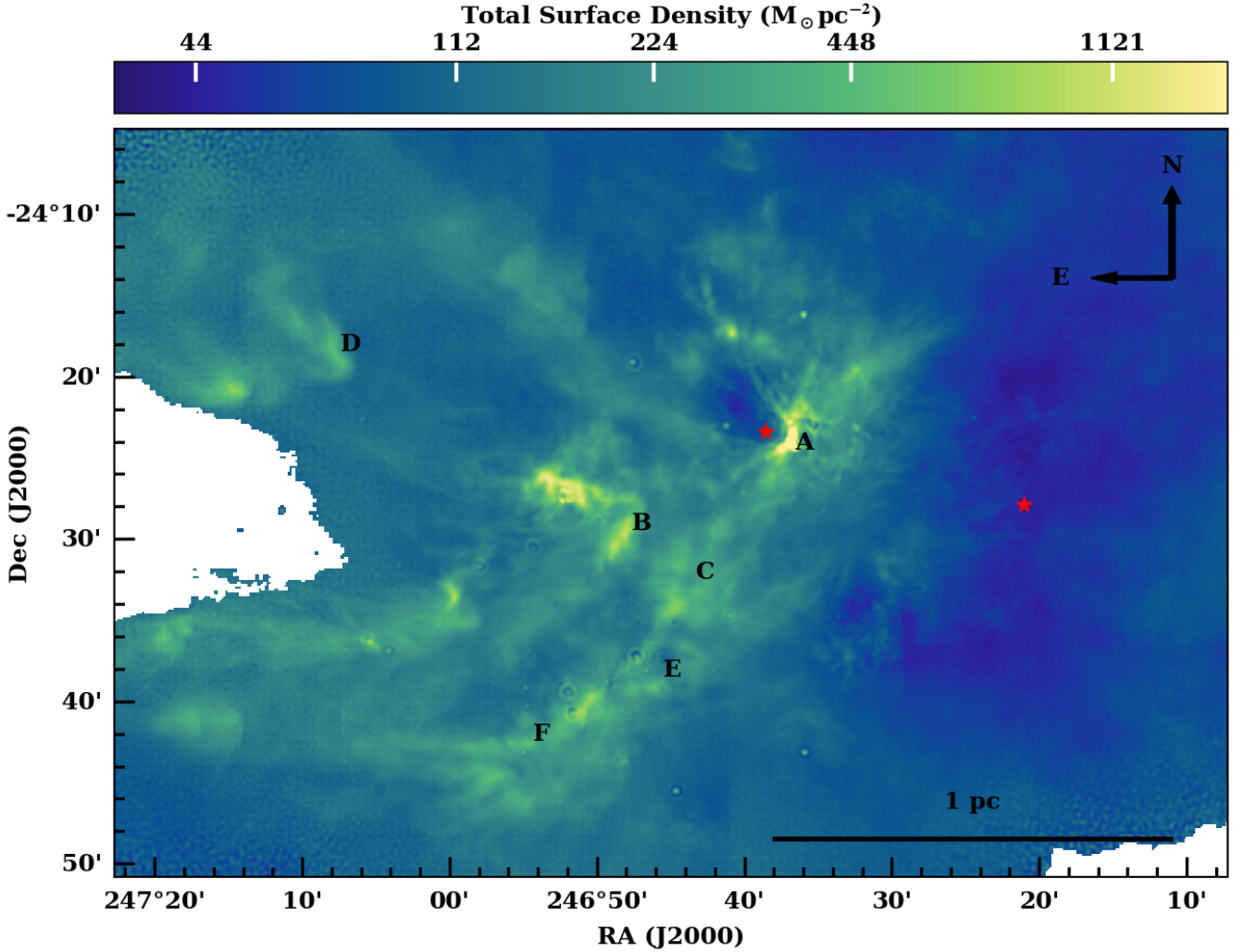


Figure 4. The estimated total surface density, Σ , for the L1688 sub-region. Red stars indicate the positions of the S1 and HD147889 pre-main sequence B stars. Letters A-F indicate the approximate positions of the dense DCO⁺ cores identified by Loren et al. (1990).

HD147889 are also clearly visible. The map of the PPSD for L1688 is given in Appendix A.

Figs. 5a and b show the mean line-of-sight dust temperature (Eq. 14) and the mean line-of-sight dust opacity index (Eq. 15) for the L1688 sub-region. Fig. 5a clearly shows the temperature gradient across the region, as well as the additional heating from S1 and HD147889. The mean temperatures of the dust in the filamentary structures seen in Fig. 4 do not generally differ greatly from those in their local surroundings, which makes them difficult to identify clearly on Fig. 5a. The exceptions are the structures associated with Rho Oph B, and, to a lesser extent, Rho Oph D, which are noticeably cooler.

The map of mean dust opacity index (Fig. 5b) does not trace the fine structure of the region as clearly as the maps of surface density (Fig. 4) or mean dust temperature (Fig. 5a). However, the dust in regions with higher surface density on Fig. 4 tends to have $\beta \lesssim 1.3$, while the dust in regions with lower surface density tends to have $\beta \gtrsim 1.7$. A similar trend of dense regions harbouring dust with a lower opacity index than the more diffuse background material was observed in Taurus by Howard et al. (2019). Proximity to the B stars

S1 and HD147889 does not appear to influence the opacity index greatly.

Fig. 6 shows a montage of images in all the wavebands used (i.e. the five *Herschel* bands at 70 μm , 160 μm , 250 μm , 350 μm , 500 μm , and the SCUBA2 band at 850 μm). The central column shows the actual observed images. The lefthand column shows synthetic images generated from the PPMAP estimates of the T - and β -differential optical depth contributions, $\Delta^2\tau_{0:k\ell}$, on the line of sight through each pixel (i.e Eq. 8). The righthand column shows synthetic images generated from the MBB estimates of the average optical depth, $\bar{\tau}_0$, and temperature, \bar{T} , on the line of sight through each pixel (i.e. Eq. 7). In all cases the images are at the native resolution of the corresponding *Herschel* image. Where the resolution of the PPMAP or MBB results is coarser than the corresponding *Herschel* image, values at the native resolution have been generated by interpolation.

To evaluate the fidelity of the results, we compute a goodness-of-fit

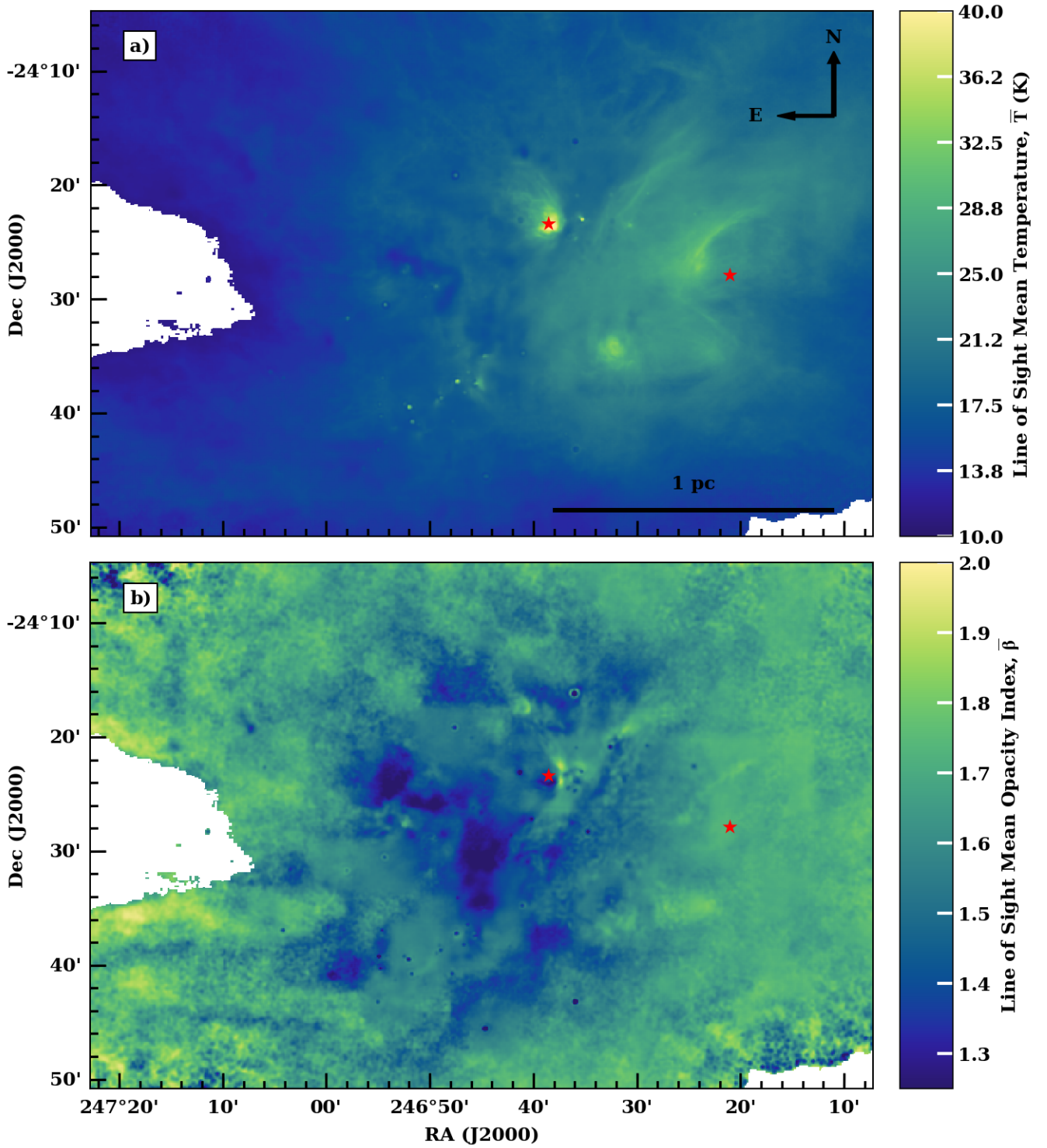


Figure 5. Maps of (a) the mean line-of-sight dust temperature (Eq. 14), and (b) the mean line-of-sight dust opacity index (Eq. 15), for the L1688 sub-region. The red stars indicate the positions of the S1 and HD147889 pre-main sequence B stars.

metric,

$$\mathcal{G}_{\text{PROC:WB}} = \left\{ \frac{\sum_{\text{PIXELS}} \left\{ I_{\text{TRUE:WB}}^{-1} [I_{\text{PROC:WB}} - I_{\text{TRUE:WB}}]^2 \right\}}{\sum_{\text{PIXELS}} \{ I_{\text{TRUE:WB}} \}} \right\}^{1/2}, \quad (16)$$

for each synthetic image (cf. Howard et al. 2019). In Eq. 16, the ' I 's are the intensities in individual pixels, the summations are over all pixels, the subscript 'PROC' stands for the procedure used to generate the synthetic intensities (i.e. PPMAP or MBB), the subscript 'TRUE'

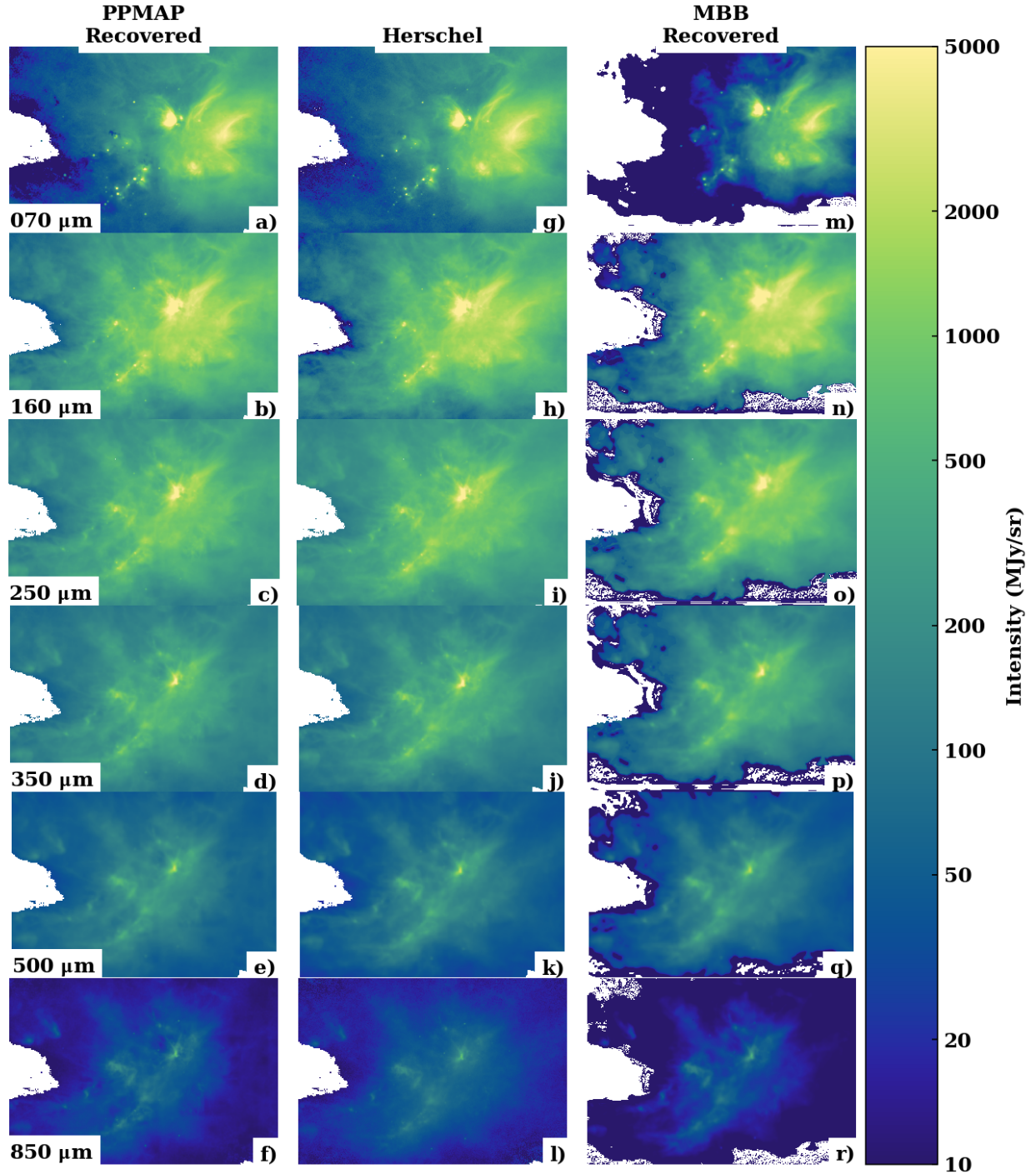


Figure 6. A montage of images of L1688. The central column shows the original images in the different *Herschel* and SCUBA2 wavebands. The lefthand column shows synthetic images derived from the PPMAP estimates of T – and β –differential optical depth (i.e. Eq. 8). The righthand column shows synthetic images from the MBB estimates of \bar{T} (i.e. Eq. 7).

stands for the actual observations, and the subscript ‘wb’ stands for the waveband under consideration. Values of \mathcal{G} are summarised in Table 1. We see that in all but one of the wavebands the PPMAP procedure produces a significantly better fit to the true observations than the MBB procedure. Moreover, in the one waveband where MBB produces the better fit (500 μm), the difference in \mathcal{G} values is small. The goodness-of-fit values, \mathcal{G} , obtained by PPMAP for Ophiuchus are

significantly worse (higher) than those reported for Taurus in Howard et al. (2019), because the Ophiuchus analysis is compromised by the very noisy edges of the mapped regions.

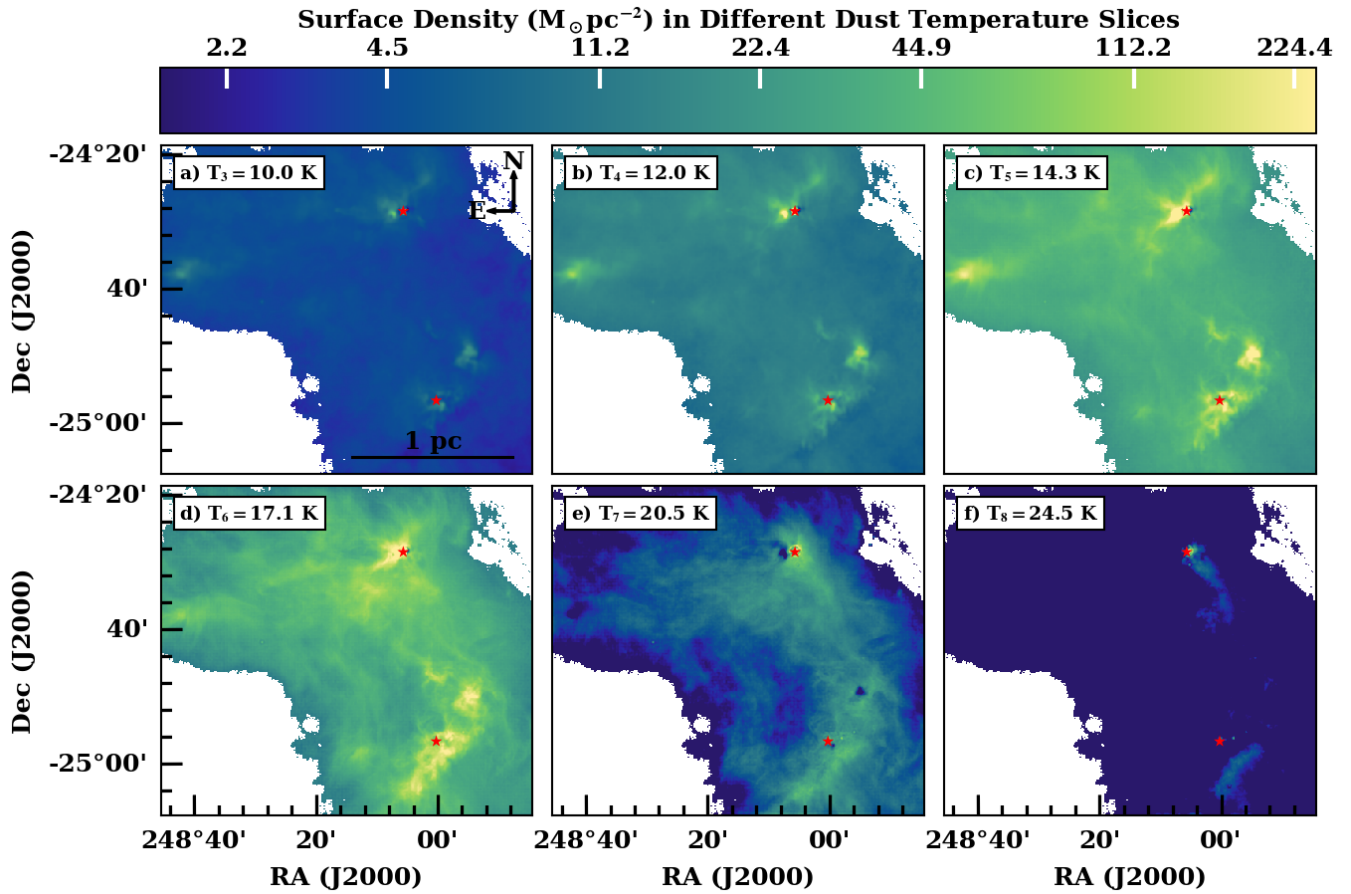


Figure 7. Six contiguous PPMAP temperature slices for the L1689 sub-region, showing the surface density, Σ , as traced by dust having temperature represented by the value marked in the top left. The red stars indicate the positions of L1689-IRS6 and 16293-2422.

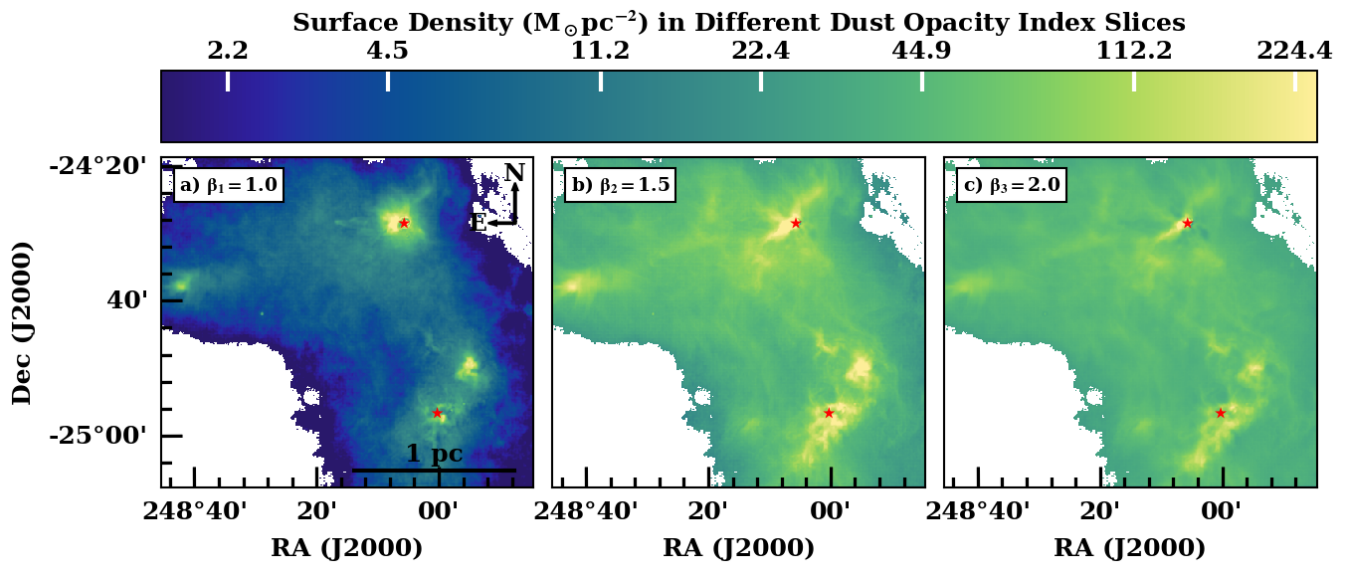


Figure 8. Three contiguous PPMAP opacity-index slices for the L1689 sub-region, showing the surface density, Σ , as traced by dust having opacity index represented by the value marked in the top left. The red stars indicate the positions of L1689-IRS6 and 16293-2422.

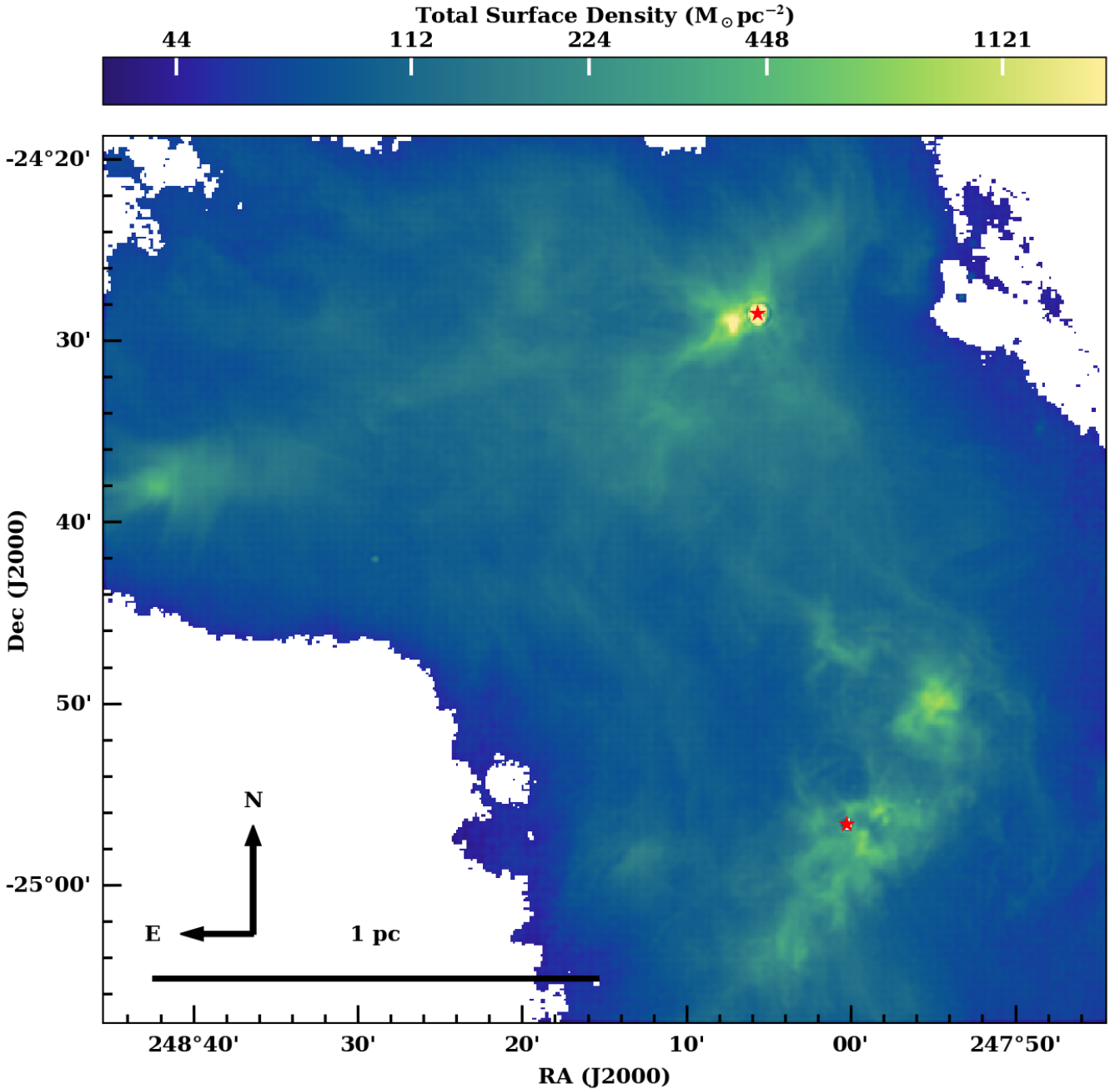


Figure 9. The estimated total surface density, Σ , for the L1689 sub-region. The red stars indicate the positions of the L1689-IRS6 and 16293-2422 protostellar systems.

5.3 L1689

Fig. 7 shows temperature slices for the L1689 sub-region of Ophiuchus at six contiguous temperatures ($T_3 = 10.0$ K, $T_4 = 12.0$ K, $T_5 = 14.3$ K, $T_6 = 17.1$ K, $T_7 = 20.5$ K and $T_8 = 24.5$ K). There are three dense, compact, and seemingly isolated structures in the temperature slices with $T \leq 12.0$ K, to the south, north and north east of the sub-region; these structures correspond to the dense clumps identified by Loren et al. (1990), respectively L1689-South, L1689-North and L1689-East. The slices at temperatures ≥ 14.3 K reveal a network of interconnecting filamentary structures between

these clumps, which are not prominent at lower temperatures. In the ≥ 17.1 K slices, L1689-East is less visible than the other two clumps, indicating that it is not as warm. Overall the dust in L1689 is colder than that in L1688, with only two small ridges of material at 24.5 K; this material is located near the masked protostellar systems, L1689-IRS6 and 16293-2422, and probably experiences additional local heating from these sources. The overall temperature difference between L1689 and L1688 is probably attributable to the earlier evolutionary state of L1689-IRS6 and 16293-2422 (as compared with S1 and HD147889), and/or to the greater distance of L1689 from the Upper Sco OB association.

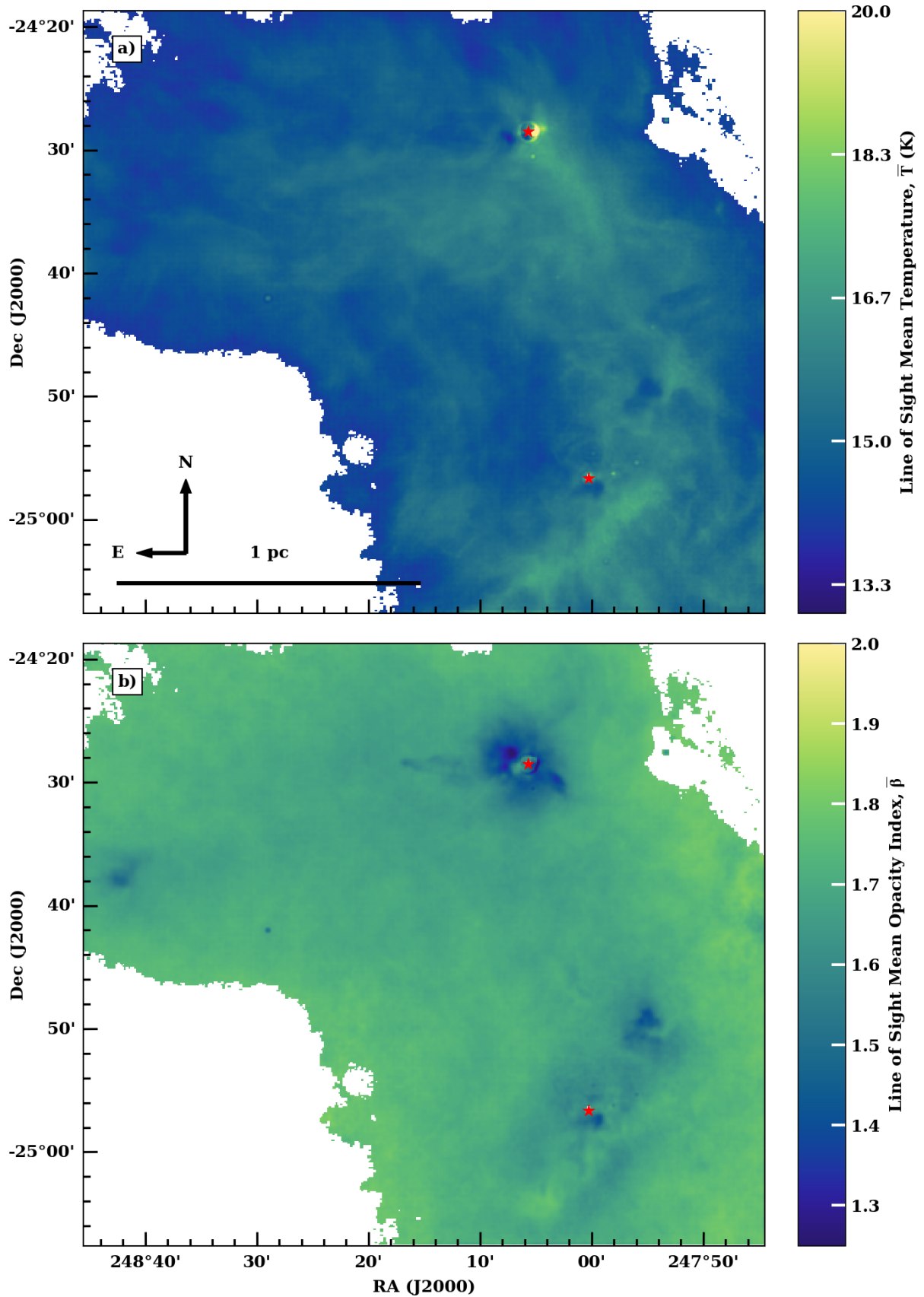


Figure 10. Maps of (a) the mean line-of-sight dust temperature (Eq. 14), and (b) the mean line-of-sight dust opacity index (Eq. 15), for the L1689 sub-region. The red stars indicate the positions of the L1689-IRS6 and 16293-2422 pre-stellar systems.

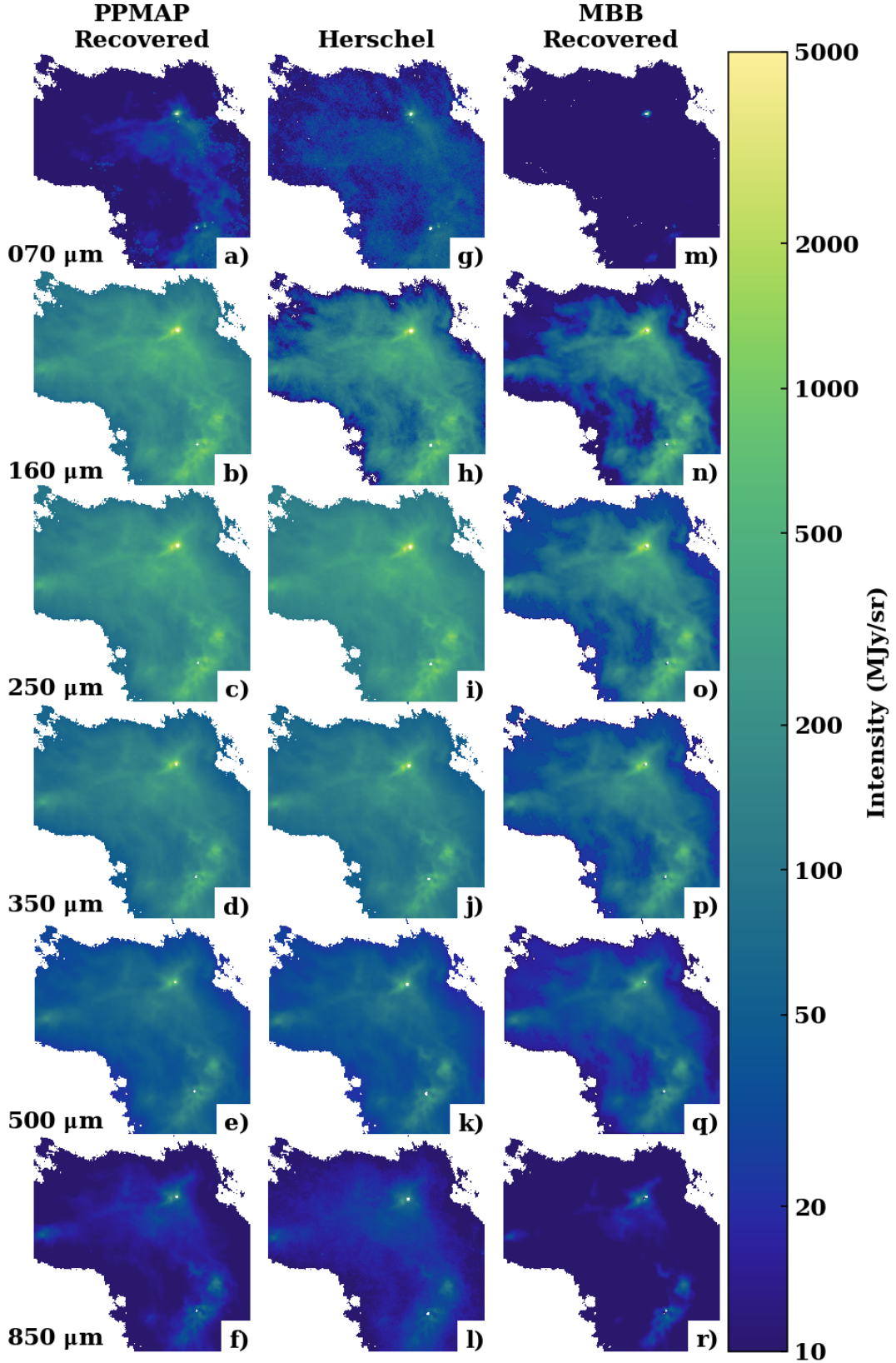


Figure 11. A montage of images of L1689. The central column shows the original images in the different *Herschel* and SCUBA2 wavebands. The lefthand column shows synthetic images derived from the PPMAP estimates of T - and β -differential optical depth (i.e. Eq. 8). The righthand column shows synthetic images from the MBB estimates of \bar{T} (i.e. Eq. 7).

Table 1. Values of the goodness-of-fit metric, \mathcal{G} (Eq. 16), for synthetic maps of the two subregions (L1688 and L1689), based on the PPMAP procedure and the MBB procedure.

SUBREGION PROCEDURE	L1688		L1689	
	PPMAP	MBB	PPMAP	MBB
WAVEBAND				
70 μm	0.21	1.21	0.57	0.97
160 μm	0.29	0.66	0.50	0.48
250 μm	0.19	0.57	0.18	0.57
350 μm	0.20	0.55	0.17	0.43
500 μm	0.28	0.21	0.28	0.30
850 μm	0.32	0.54	0.32	0.56

Fig. 8 shows the opacity-index slices for the L1689 sub-region for all three discrete values of β . As with L1688, a much larger proportion of the material in the $\beta = 1.0$ slice is found within the central regions of the dense, cold clumps than in the surrounding medium. This diffuse medium is better traced by material with a higher opacity index.

Fig. 9 shows the estimated total surface density, Σ , derived from Eqns. (4) and (11). The L1689-South, L1689-North and L1689-East clumps are still clearly visible, although the network of diffuse interconnecting filamentary structures is less apparent than in Fig. 7. The map of the PPSD for L1689 is given in Appendix A.

Figs. 10a and b show the mean line-of-sight dust temperature (Eq. 14) and the mean line-of-sight dust opacity index (Eq. 15), for the L1689 sub-region. On Fig. 10a, the dense clumps (L1689-South, L1689-North and L1689-East) and the interconnecting filamentary structures appear to be somewhat warmer (~ 17 K) than the more diffuse surroundings (~ 14 K). There are several possible explanations for this seemingly paradoxical result, all of which relate to the fact that the line-of-sight averaging combines contributions from different regions along the line of sight with different radiation fields, and also contributions from different types of dust which may co-exist in the same volume. One explanation is that the lines of sight away from the dense clumps have significant contributions from regions that are not close to Ophiuchus, and as a consequence have a weaker background radiation field and cooler dust; a threefold reduction in the ambient radiation field would reduce the equilibrium temperature of a typical dust grain (of the same type) from ~ 17 K to ~ 14 K. A second explanation is that there is significant extra dust heating within the clumps, due to embedded or nearby sources (including L1689-IRS6 and 16293-2422); on Fig. 7f (the $T_8 = 24.5$ K panel) there is evidence for local heating fronts to the south-west of L1689-North and to the south-west of L1689-South.

Fig. 10b shows the mean line-of-sight opacity index for the L1689 sub-region. As in L1688, the diffuse dust has a relatively high mean opacity index, $\bar{\beta} \gtrsim 1.7$, while the dust in the denser regions has a lower value, $\bar{\beta} \lesssim 1.4$.

Fig. 11 shows a montage of images of L1689, equivalent to those in Fig. 6. The goodness-of-fit metric, \mathcal{G} (see Eq. 16) for each synthetic image is given in Table 1. Again, in all but one waveband the PPMAP procedure produces a significantly better fit than the MBB procedure. In the one waveband where this is not the case (160 μm), the PACS images are very noisy in the low-intensity regions and the \mathcal{G} values are very similar.

6 THE MASS DISTRIBUTION IN L1688 AND L1689

The PPMAP pixels have angular size $\Delta\Omega_{\text{pixel}} = 49 \text{ arcsec}^2$, and Ophiuchus is assumed to be at $D = 140 \text{ pc}$. Hence, from Eq. (6), the mass

in a single pixel is

$$\Delta M_{\text{pixel}} \sim 1.1 M_{\odot} \tau_0. \quad (17)$$

Since the uncertainties in this conversion are dominated by the mass opacity ($\propto \kappa_0^{-1}$) and the distance ($\propto D^2$), we do not quote the PPMAP uncertainties (which are much smaller, see Appendix A) and we give all masses and surface densities to two significant figures. Even this is unduly optimistic for absolute values, but relative values should be more reliable. The results are summarised in Table 2.

Summing the pixels on Fig. 4, the estimated mass and mean surface density of the L1688 sub-region (the region outlined in black on Fig. 1) are $650 M_{\odot}$ and $110 M_{\odot} \text{ pc}^{-2}$. The corresponding quantities for L1689 (Fig. 9) are $400 M_{\odot}$ and $66 M_{\odot} \text{ pc}^{-2}$.

However, the rectangular boundaries defining the sub-regions are somewhat arbitrary. In order to make our analysis more objective, we focus on the *High Efficiency Regions* (HERs) of L1688 and L1689. The HERs are the regions with surface density $\Sigma > \Sigma_{\text{T}} \approx 160 M_{\odot} \text{ pc}^{-2}$ (and hence $A_{\text{V}} > A_{\text{T}} \approx 7 \text{ mag}$). Several studies (e.g. André et al. 2010; Lada et al. 2010; Könyves et al. 2015) have found that this threshold column density marks an abrupt transition to high star formation efficiency. Figs. 12 and 13 show maps of Σ (the same as Figs. 4 and 9), with the boundaries of the HERs marked in black. The mass, area and mean surface density of the L1688 HER are $290 M_{\odot}$, 1.2 pc^2 and $240 M_{\odot} \text{ pc}^{-2}$. For the L1689 HER, these quantities are $89 M_{\odot}$, 0.37 pc^2 and $240 M_{\odot} \text{ pc}^{-2}$. The masses derived here are lower than those obtained by Ladjelate et al. (2020) because their MBB fit returns a single, flux-averaged mean temperature along each line of sight. Consequently it overestimates the contribution from hotter than average dust, and underestimates the contribution from colder than average dust. Marsh et al. (2015) have shown that, when using a flux-averaged mean, the overestimate usually dominates, and therefore total masses are often overestimated – sometimes by as much as 100%, but here by $\sim 50\%$.

To analyse the population of starless and pre-stellar cores in L1688 and L1689, we use the catalogue of Ladjelate et al. (2020), which identifies 513 cores in Ophiuchus, and fits them with ellipses.⁶ 49 of these cores are identified as protostellar. Consequently they are optically thick, and PPMAP cannot fit them. Of the remaining 464 starless and pre-stellar cores, 288 lie in the L1688 sub-region, and 101 in the L1689 sub-region. The elliptical fits for these cores are shown in white on Figs. 12 and 13.

We estimate the masses of the starless and pre-stellar cores by applying the `photutils` Python package (Bradley et al. 2016) to the maps of total H_2 column density, using elliptical apertures corresponding to the fits given by Ladjelate et al. (2020). The 288 cores in the L1688 sub-region have a combined mass of $100 M_{\odot}$, and thus account for 16% of the total mass of the sub-region. The 101 cores in the L1689 sub-region have a combined mass of $(41.0 \pm 0.1) M_{\odot}$, making up 10% of the total mass of the sub-region.

Figs. 12 and 13 show that the majority of the cores lie within the HERs. By excluding the cores that lie outside of the HERs in L1688, we find the remaining 219 cores have a total mass of $84 M_{\odot}$, which accounts for 29% of the HER mass. In L1689, the 81 cores found within the HER contain $32 M_{\odot}$, or 36% of the HER mass. These

⁶ The convention we have adopted is that ‘starless cores’ are cores that do not contain stars and appear not to be gravitationally bound; they are therefore likely to disperse unless their circumstances change, for example some other force acts to contain them or they increase their mass by accretion or merger. Conversely, ‘pre-stellar cores’ are cores that do not contain stars but appear to be gravitational bound; they are therefore expected to collapse and form a single star, or a multiple system, or a small sub-cluster of stars.

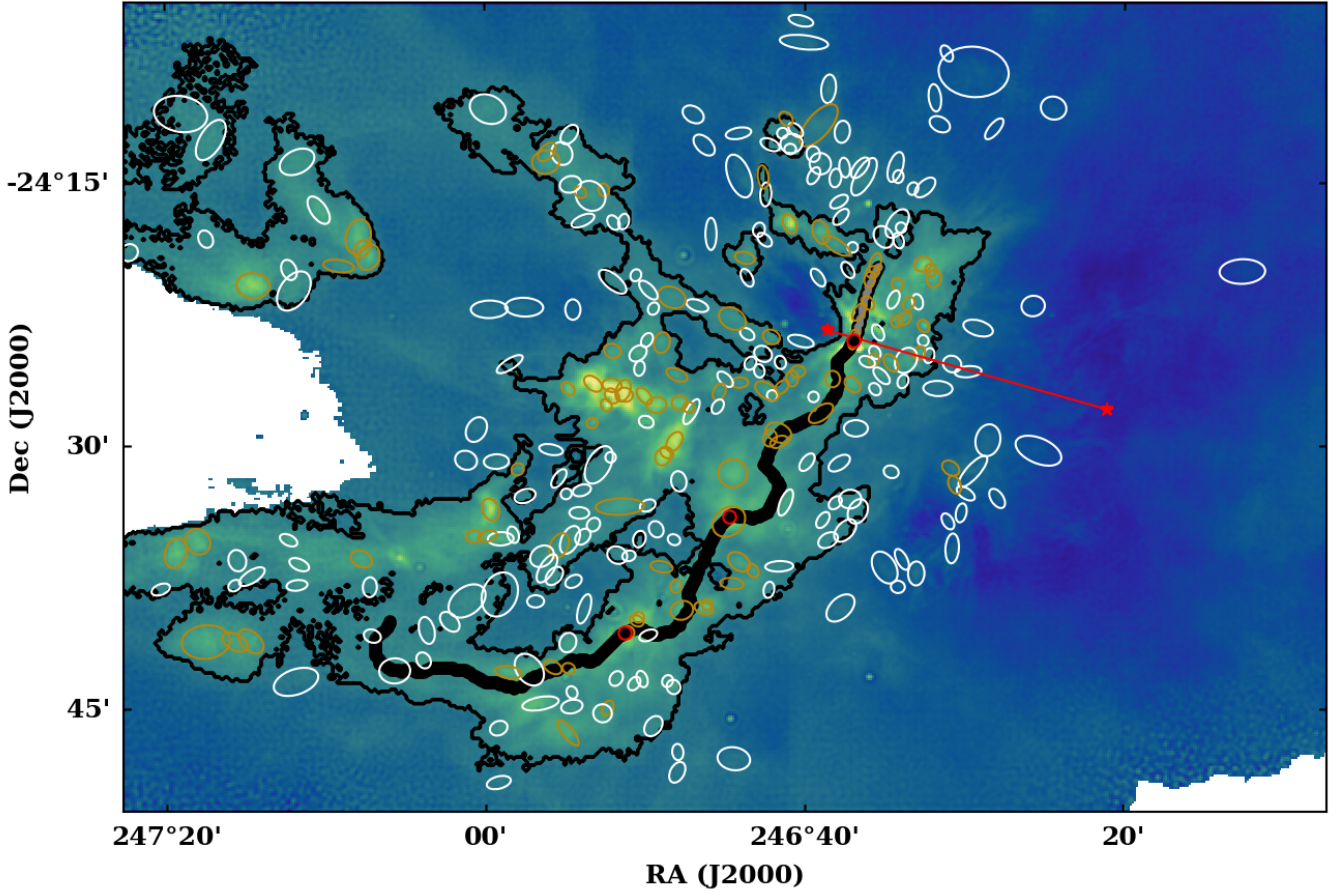


Figure 12. The total surface density, Σ , for L1688 (as Fig. 4) with the High Efficiency Regions (HERs) outlined in **black**, and the starless and pre-stellar cores identified by Ladjelate et al. (2020) shown as, respectively, white and gold ellipses. The red stars mark the locations of the B stars S1 and HD147889, and the red line connecting them (the S1-HD147889 axis) is discussed further in Section 7.4. Filament f1 is traced with black filled circles. The red outlined circles represent local column density maxima along the filament spine.

percentages are higher than those reported by Ladjelate et al. (2020), firstly because the masses we derive for the HERs are lower, as explained above, and secondly because we have summed the masses of all cores, starless and prestellar.

Thus, the fraction of the total mass in the L1688 sub-region that is in cores is 50% times higher than in the L1689 sub-region. In contrast, the fraction of the total mass in the L1688 HER that is in cores is much closer to – and actually 20% lower than – the fraction in the L1689 HER. This suggests that the core formation efficiency is more strongly dependent on local surface density than total cloud mass.

Essentially the same trends are found if we use the core masses obtained by Ladjelate et al. (2020) using modified black body fits to the *Herschel* observations, or the core masses obtained by Nutter et al. (2006) using both a different method of mass estimation and a different core catalogue.

We confirm the existence of a threshold surface density, Σ_T , for efficient star formation by repeating the above analysis with different values for Σ . Following the procedure outlined in Könyves et al. (2015), we vary Σ and compute the efficiency,

$$\eta(\Sigma) = \frac{M_{\text{CORES}}(\Sigma)}{M_{\text{TOTAL}}(\Sigma)}, \quad (18)$$

where $M_{\text{CORES}}(\Sigma)$ is the net mass of cores inside the iso-contour at

Σ and $M_{\text{TOTAL}}(\Sigma)$ is the total mass of everything (cores and intercore material) inside the iso-contour at Σ . Fig. 14 shows $\eta(\Sigma)$, on a log-log scale, for the L1688 sub-region (blue) and the L1689 sub-region (orange). The thin curves are for prestellar cores alone, and the thick curves are for starless and prestellar cores combined. These plots support the suggestion that there is a threshold surface-density above which the conversion of interstellar gas into prestellar cores is highly efficient, and below which it is very inefficient (Könyves et al. 2015). In Ophiuchus, the threshold appears to be at $\Sigma_T \sim 270(\pm 40) M_{\odot} \text{pc}^{-2}$ (corresponding to $A_V \sim 12(\pm 2)$); this is the surface density above which prestellar cores contribute more mass than starless cores. It is somewhat higher than the $\Sigma_T \sim 160 M_{\odot} \text{pc}^{-2}$ (corresponding to $A_V \sim 7$) estimated by Könyves et al. (2015). There may be local variations in the threshold, reflecting for example the intensity of the local radiation field. However, we should also keep in mind that our estimate is based on small-number statistics, and that there is uncertainty in how a prestellar core should be defined.

A related issue is what is likely to happen to the starless cores in the future. In the theory of turbulent fragmentation, it is inevitable that a significant fraction of starless cores are sterile, in the sense that they do not become prestellar, and therefore do not spawn stars (Padoan & Nordlund 2002). These sterile cores either have too little mass to be strongly self-gravitating, or they are compressed too little

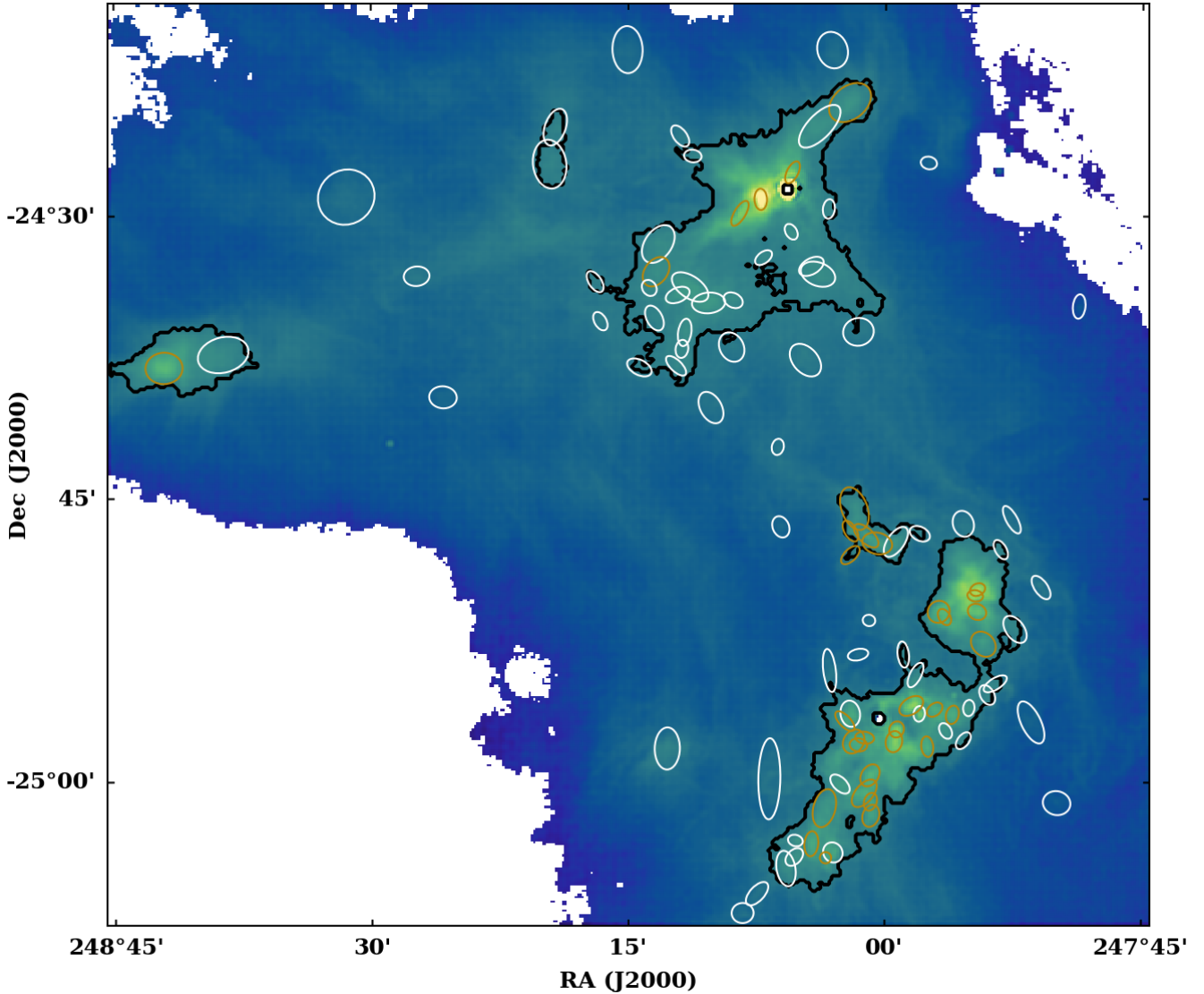


Figure 13. The total surface density, Σ , for L1689 (as Fig. 9) with the High Efficiency Regions (HERs) outlined in **black**, and the starless and pre-stellar cores identified by Ladjelate et al. (2020) shown as, respectively, white and gold ellipses.

(by the ram-pressure of the flows creating them and/or by the background gravitational field), and they disperse. As noted previously by André et al. (2010), André et al. (2014) and Ladjelate et al. (2020), in Ophiuchus – and also in many other star formation regions – the conditions for forming prestellar cores exist, almost exclusively, in filaments. Presumably the large-scale converging flows creating a filament deliver a reservoir of mass from which nascent cores can continue to accrete, a large ram-pressure to compress the gas, and a background gravitational field that will inhibit re-expansion. Conversely, cores that form in relative isolation, outside a filament, are much less likely to spawn stars; they have less ambient gas to accrete, lower external pressure, and no assistance from the collective gravitational field of a filament.

We suggest that many of the starless cores observed in Ophiuchus are indeed destined to disperse. On Fig. 15 we plot the cumulative distributions of D_{C2F} (Fig. 15a) and $\mathcal{R} = D_{\text{C2F}}/r_{\text{C}}$ (Fig. 15b), where D_{C2F} is the projected distance from a core to the nearest filament spine-point, $r_{\text{C}} = (ab)^{1/2}$ is the mean radius of the core, a and b are

the semi-major and semi-minor axes of the fitted elliptical outline of the core from Ladjelate et al. (2020). The thick curves represent the prestellar cores, and the thin curves represent the starless cores; blue curves represent L1688, and orange ones represent L1689. The timescale for a starless core to disperse is $t_{\text{disp}} \lesssim r_{\text{C}}/c_{\text{s}}$, where c_{s} is the sound speed (typically $0.25 \pm 0.05 \text{ km s}^{-1}$, corresponding to gas-kinetic temperatures between $\sim 11 \text{ K}$ and $\sim 26 \text{ K}$), and ‘ \lesssim ’ is used because the core may already be dispersing. Conversely, the timescale for a starless core to shift to a filament is $t_{\text{shift}} \gtrsim D_{\text{C2F}}/Mc_{\text{s}}$, where M is the Mach Number of the core’s bulk velocity and ‘ \gtrsim ’ is used because the bulk velocity must also be directed towards the nearest filament. A starless core is only likely to become prestellar if either a new filament forms around it, which seems unlikely, or it shifts to an existing filament on a timescale $t_{\text{shift}} < t_{\text{disp}}$, which requires $M > \mathcal{R}$. The offset between the medians of the cumulative distributions on Fig. 15b is $\mathcal{R} \sim 5$. This implies that very few of the starless cores are likely to reach one of the existing filaments before dispersing,

unless they have bulk velocities with $\mathcal{M} > 5$ ($v > 1 \text{ km s}^{-1}$), and this velocity is directed towards, or close to, the nearest part of that filament, which again seems unlikely.

To be more specific, we consider the starless cores on the 25th percentile of the distribution of D_{C2F} values, which are at a projected distance $D_{\text{C2F};25\%} \sim 0.5 \text{ pc}$ from the nearest filament (see Fig. 15a). If these cores have a mean radius of $r_{\text{C}} \sim 0.05 \text{ pc}$ and isothermal sound speed $c_{\text{S}} \sim 0.2 \text{ km s}^{-1}$, they will disperse on a timescale $t_{\text{disp}} \sim 0.25 \text{ Myr}$. They must have a bulk velocity $v > 2 \text{ km s}^{-1}$ to reach the filament before they disperse. The lower limit on v is justified on two counts: first, because the actual distance is greater than the projected distance; and second, because the starless core may not be moving towards the nearest point on the filament. Moreover, even if the nearest filament is infinitely long, and if it has a diameter of 0.6 pc , it only subtends a solid angle $\Omega = \pi(0.6 \text{ pc}/(0.5 \text{ pc}))$, i.e. 30% of the sky, so if the bulk velocity of the starless core is randomly oriented, it has only a 30% chance of ever reaching the filament.

It is appropriate to consider whether the above estimate should be modified to take account of gravity, which will both accelerate the bulk motion of the core towards the filament, and deflect its trajectory towards the filament (gravitational focussing). The gravitational potential outside a straight filament with line-density μ is $\phi(r) = 2G\mu \ln(r/r_{\text{B}})$, where r is the radial distance from the spine of the filament, and r_{B} is the boundary radius of the filament. If, for the purpose of illustration, we adopt (i) a transcritical filament with $\mu = \mu_{\text{CRIT}} = 2c_{\text{S}}^2/G \sim 16 M_{\odot} \text{ pc}^{-1}$ (where we have substituted $c_{\text{S}} = 0.2 \text{ km s}^{-1}$, appropriate for molecular gas at temperature $T \sim 10 \text{ K}$), and (ii) and the canonical $r_{\text{B}} \sim 0.3 \text{ pc}$, then $\phi(r) \sim 4c_{\text{S}}^2 \ln(r/0.3 \text{ pc}) \sim 0.16 \text{ km}^2 \text{ s}^{-2} \ln(r/0.3 \text{ pc})$. It follows that a starless core which starts off at $r = D_{\text{C2F};25\%} \sim 0.5 \text{ pc}$ with velocity $v > 2 \text{ km s}^{-1}$ directed towards a nearby filament acquires an extra velocity $\Delta v = (G\mu_{\text{CRIT}}/v) \ln(D_{\text{C2F};25\%}/r_{\text{B}}) < 0.02 \text{ km s}^{-1}$, which can safely be ignored compared with $v > 2 \text{ km s}^{-1}$. Even if we consider the maximum line-density for the filaments in Ophiuchus, $\mu_{\text{MAX}} \sim 100 M_{\odot} \text{ pc}^{-1}$ (see Fig. 5A in Arzoumanian et al. (2019)), the velocity increases by at most 0.2 km s^{-1} , which is still small. Gravitational focussing is not important.

It follows that a core in a filament is effectively trapped by the gravitational potential well of the filament. Its specific thermal energy $3c_{\text{S}}^2/2 \sim 0.06 \text{ km}^2 \text{ s}^{-2}$ is insufficient to escape from the gravitational potential of the filament. Such cores also have access to a large reservoir of material from which to accrete, and a large external pressure to inhibit their dispersal.

Conversely, many of the starless cores outside of filaments are probably transient condensations that will disperse. Because they are not in filaments, they do not have a large nearby reservoir of material from which to accrete, they do not have a very large external pressure to inhibit their dispersal, and they also do not have the background gravitational field of a filament to inhibit their dispersal.

7 ANALYSIS OF THE NETWORK OF FILAMENTS IN RHO OPH

7.1 Identifying filaments

To analyse the networks of filamentary structures visible in the surface density maps, we apply the FilFinder algorithm (Koch & Rosolowsky 2015), with the minimum threshold (`g1ob_thresh`) set to five times the median background noise (i.e. $\Sigma > 180 M_{\odot} \text{ pc}^{-2}$ for L1688, and $\Sigma > 135 M_{\odot} \text{ pc}^{-2}$ for L1689) and the minimum structure area (`size_thresh`) set to 400 pixels (equivalent to 0.009 pc^2).

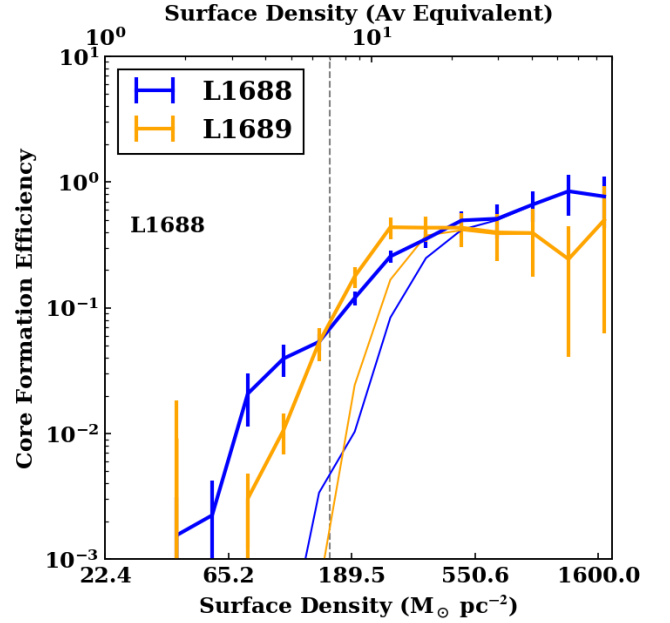


Figure 14. Log-log plot of the core formation efficiency, η , as a function of the threshold surface density, Σ (Eq. 18). *Blue curves:* L1688. *Orange curves:* L1689. *Thick curves:* starless and prestellar cores together. *Thin curves:* prestellar cores alone. The vertical dashed line marks the threshold, $\Sigma_{\text{T}} \sim 160 M_{\odot} \text{ pc}^{-2}$, estimated by Könyves et al. (2015); these results suggest that in Ophiuchus the threshold may be a little higher, $\Sigma_{\text{T}} \sim 270 M_{\odot} \text{ pc}^{-2}$.

Next we prune each filament of its branches, leaving the longest path through the filament to trace its spine. Finally we discard filaments shorter than 0.3 pc . These are the selection criteria proposed by Arzoumanian et al. (2011), with a view to ensuring that all filaments have an aspect ratio ≥ 3 , assuming a width of 0.1 pc . We find six filaments satisfying these criteria in L1688, and three in L1689. The spines of these filaments, along with unique identifiers, are traced on Figs. 16a and 16d. FilFinder finds a loop near the middle of the g2 filament in L1689, which appears to trace the intersection of the filament with the edge of a clump; the loop is shown with a dashed black line on Fig. 16d. In the sequel we exclude the loop and analyse the two parts on either side of the loop separately, as g2a and g2b.

We note that in L1688, all six filaments lie within the HERs (shown in Fig. 16a and 16d by the grey contours). In L1689, however, only g1 and g2a are completely within HERs. Approximately half of g3 extends beyond the HER associated with L1689-East, while g2b falls in the lower density region between L1689-East and L1689-North.

7.2 Fitting filament profiles

To quantify the properties of the filaments, we first define discrete spine points equally spaced at intervals of $7''$ ($\sim 0.005 \text{ pc}$) along the spine of each filament. Next we determine the local tangent to the spine at each spine point by spline fitting. We then compute the column density, at discrete values of the impact parameter, b , along the line through the spine point and orthogonal to the local tangent. This gives a local column density profile for each spine point – albeit a rather noisy one.

Table 2. The distribution of mass in L1688 and L1689. In each case we give values for the whole sub-region (as defined by the rectangular outlines on Fig. 1) and for the HERs (which are the regions with surface density exceeding $160 M_{\odot} \text{pc}^{-2}$, marked with black contours on Figs. 12 and 13. *First row:* the total mass of gas and dust in the region (excluding protostars). *Second row:* The total area of the region. *Third row:* the mean surface density of the region. *Fourth row:* the number of starless and prestellar cores. *Fifth row:* The net mass of starless and prestellar cores. *Sixth row:* The fraction of mass in starless and prestellar cores.

	L1688		L1689	
	SubR	HER	SubR	HER
Total mass	$650 M_{\odot}$	$290 M_{\odot}$	$400 M_{\odot}$	$89 M_{\odot}$
Total area	5.7 pc^2	1.2 pc^2	6.0 pc^2	0.37 pc^2
Mean surface-density	$110 M_{\odot} \text{ pc}^{-2}$	$240 M_{\odot} \text{ pc}^{-2}$	$66 M_{\odot} \text{ pc}^{-2}$	$240 M_{\odot} \text{ pc}^{-2}$
Number of cores	288	219	101	81
Net mass of cores	$100 M_{\odot}$	$84 M_{\odot}$	$41 M_{\odot}$	$32 M_{\odot}$
Fraction of mass in cores	16%	29%	10%	36%

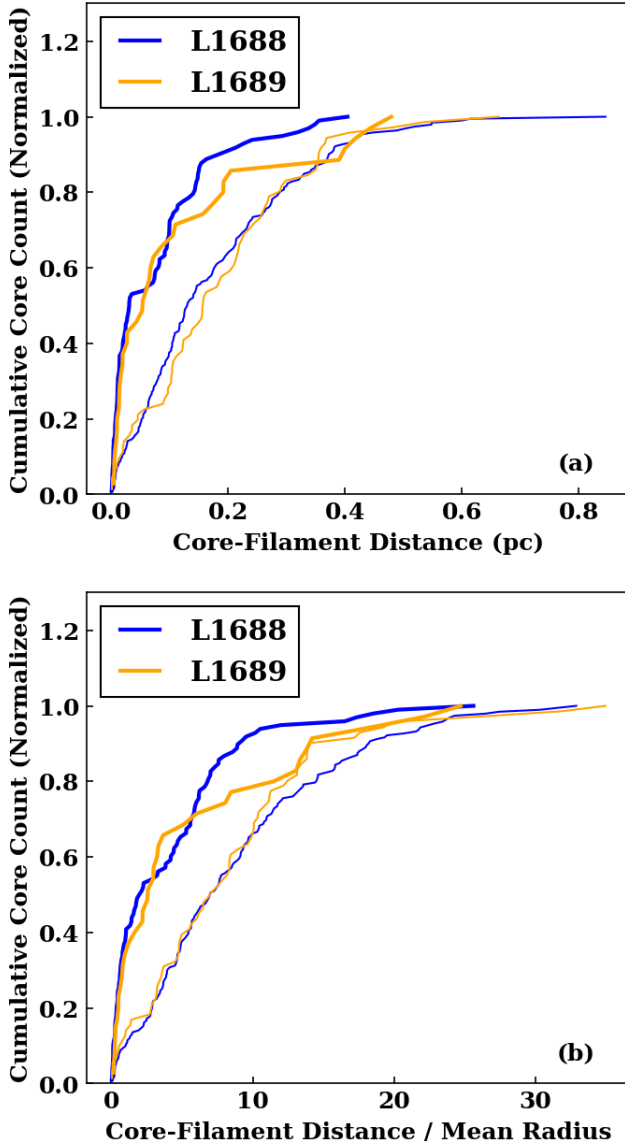


Figure 15. The cumulative distributions of (a) D_{C2F} (the projected distance from a core to the nearest filament spine point) and (b) $\mathcal{R} = D_{\text{C2F}}/r_{\text{C}}$ (where r_{C} is the mean radius of the core). *Blue curves:* L1688. *Orange curves:* L1689. *Thick curves:* prestellar cores. *Thin curves:* starless cores.

Finally we apply the FilChaP⁷ algorithm (Suri et al. 2019) to each of the filaments in turn. FilChaP divides a filament up into segments, where each segment is constructed from the average of 12 contiguous local profiles. This greatly improves the signal-to-noise, while retaining the spatial variations in the filament properties that would otherwise be lost by averaging all the local profiles along the entire filament length. The positions of these segments are marked by the coloured circles on Fig. 16.

FilChaP performs a background subtraction for each segment, and fits the remaining column-density profile with a Plummer-like profile (Whitworth & Ward-Thompson 2001),

$$\Sigma(b) = \Sigma_0 \left\{ 1 + \left(\frac{b}{r_0} \right)^2 \right\}^{-\frac{p-1}{2}}. \quad (19)$$

Here $\Sigma(b)$ is the column density at impact parameter b , Σ_0 is the column density on the spine, r_0 is the radius within which the volume density of the filament is approximately uniform, and p is the radial density exponent outside radius r_0 . For this study we have fixed $p = 2$ (see Palmeirim et al. (2013), Arzoumanian et al. (2019) and Howard et al. (2019) for a discussion of this choice, and Nakamura & Umemura (1999) for a theoretical justification in terms of similarity solutions for the collapse of an approximately isothermal filament). We stress that $\Sigma(b)$, and hence also Σ_0 and r_0 , are background-subtracted parameters of the filaments. FilChaP estimates the local line-density of the filament, μ , by summing explicitly the contributions to the background-subtracted filament profile (not by integrating the fitted profile, Eq. 19).

Once FilChaP has returned estimates of Σ_0 , r_0 and μ , for each segment along a filament, we compute the local $\text{FWHM} = 2(2^{1/2} - 1)^{1/2} r_0 = 1.287 r_0$, and this is plotted on Figs. 16a (L1688) and 16d (L1689). The median FWHM of all the filaments in L1688 is $(0.11 \pm 0.04) \text{ pc}$, while the median FWHM of the L1689 filaments is $(0.19 \pm 0.08) \text{ pc}$. However, the filament segments that fall outside the HERs in L1689 are significantly and systematically wider than those sections within the HERs. If we exclude these low density segments, the median filament FWHM in L1689 decreases to $(0.14 \pm 0.05) \text{ pc}$. These median FWHM s are larger than those found by Howard et al. (2019) for the Taurus L1495 filament. The median FWHM s of the filaments are given in Table 3, and span a wide range from $(0.066 \pm 0.002) \text{ pc}$ for f4 in L1688, to $(0.315 \pm 0.008) \text{ pc}$ for g2b in L1689. We note that the FWHM s we find are significantly larger than those estimated by Arzoumanian et al. (2019), who find a mean and standard deviation of $0.06 \pm 0.02 \text{ pc}$ in Ophiuchus; the reason for this difference is unclear.

The values of Σ_0 for each segment are shown in Fig. 16b for

⁷ <https://github.com/astrosuri/filchap>

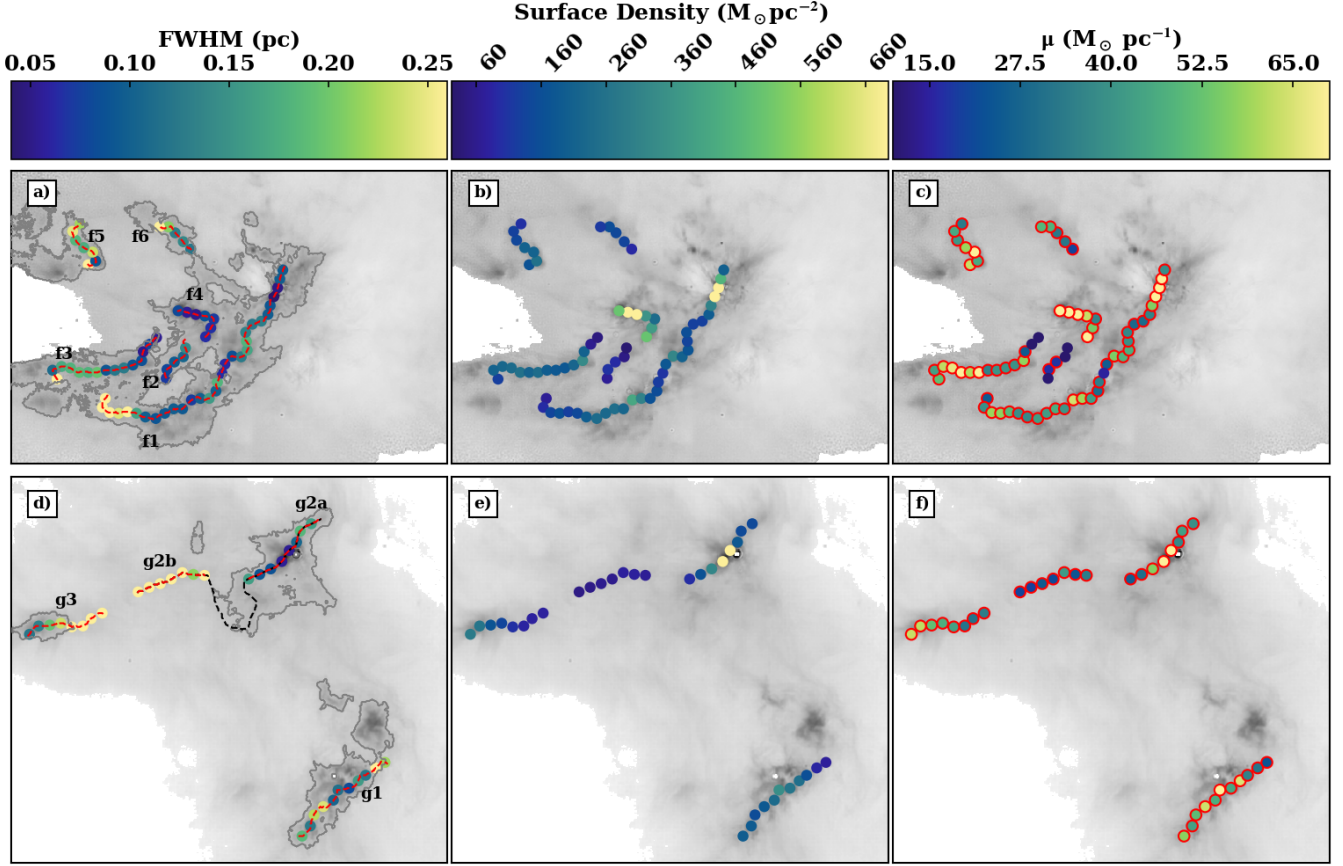


Figure 16. Filament parameters for each segment. *Top row (a-c):* L1688. *Bottom row (d-f):* L1689. *Left column (a,d):* colour-coded FWHM for each segment. *Middle column (b,e):* colour-coded surface density on spine, Σ_0 . *Right column (c,f):* colour-coded line-density, μ .

Table 3. The properties of each of the filaments identified in the L1688 and L1689 sub-regions. Σ_0 , FWHM and μ are length averaged median values.

L1688				
Fil	Σ_0 ($M_\odot \text{pc}^{-2}$)	FWHM (0.1 pc)	μ ($M_\odot \text{pc}^{-1}$)	Length (pc)
f1	185±8	1.00±0.04	42±2	1.76
f2	70±4	0.95±0.02	10.5±1.4	0.28
f3	215±4	1.21±0.08	43.6±4.5	0.81
f4	506±21	0.66±0.02	70.1±5.9	0.35
f5	171±6	2.21±0.06	46.0±4.7	0.35
f6	139±3	1.39±0.03	32.8±5.7	0.24
L1689				
Fil	Σ_0 ($M_\odot \text{pc}^{-2}$)	FWHM (0.1 pc)	μ ($M_\odot \text{pc}^{-1}$)	Length (pc)
g1	195±7	1.58±0.08	46.9±3.5	0.61
g2a	179±8	0.98±0.07	41.3±4.4	0.46
g2b	62±2	3.15±0.08	23.8±1.3	0.36
g3	122±7	2.60±0.03	45.4±4.4	0.42

L1688, and Fig. 16e for L1689. Filament f4 clearly has a higher average central column density than any of the other filaments in either sub-region. Filament f1 in L1688 and filament g2a in L1689 both contain a small number of contiguous segments which exhibit a much higher central column density than the rest of the filament. For f1, these segments are located near the line connecting the

stars S1 and HD147889, indicating that local feedback from these B stars may be significantly squeezing the filament at this location, enhancing its column density; this possibility is discussed further in Section 7.4 below. The more dense segments in g2a are located near 1689-IRS6, which may indicate that local feedback is also a factor in the density increase there. Filament g2b and the segments of g3 that lie outside the HERs show a decrease in central density which mirrors the increase in filament width discussed previously. The median central column density of each of the filaments is listed in Table 3.

7.3 Filament line-densities

Figs. 16c and 16f show the line-densities, μ , for the filament segments in L1688 and L1689, respectively. The median segment line-density in L1688 is $47 M_\odot \text{pc}^{-1}$, with a 32/68-percentile range of $\pm 18 M_\odot \text{pc}^{-1}$. The median segment line-density in L1689 is $46 M_\odot \text{pc}^{-1}$, with a 32/68-percentile range of $\pm 15 M_\odot \text{pc}^{-1}$. The 32/68-percentile range is equivalent to the standard deviation for a Gaussian distribution, and thus acts as the standard deviation for a median value. The median line densities for each filament are listed in Table 3.

If we assume that the gas is isothermal with isothermal sound speed $c_s = 0.19 \text{ km s}^{-1}$ (corresponding to molecular gas at 11 K), the critical line-density (Ostriker 1964; Inutsuka & Miyama 1997) is

$$\mu_c = \frac{2c_s^2}{G} \approx 16.2 M_\odot \text{pc}^{-1}. \quad (20)$$

In the absence of other support mechanisms (e.g., magnetic fields or turbulence), isothermal filaments with $\mu > \mu_c$ should collapse and fragment under gravity. In Figs. 16c and 16f, we outline segments with $\mu > \mu_c$ in red. This implies that all the filaments in both sub-regions are super-critical, and – in the absence of other support mechanisms – highly prone to collapse and fragmentation. However, the Green Bank Ammonia Survey finds that the median gas-kinetic temperature of dense cores in L1688 is $17.5(\pm 5.3)$ K (Kerr et al. 2019), and we might expect that the somewhat less dense gas in the filaments to be even warmer. The dust temperatures returned by PPMAP are also significantly higher than 10 K, but the densities in the filaments analysed here are probably too low for close thermal coupling between gas and dust. If the gas temperature is 25 K ($c_s = 0.30 \text{ km s}^{-1}$), then $\mu_c = 40.5 M_\odot \text{pc}^{-1}$, and just 56% of the segments in L1688, and 51% of the segments in L1689, are super-critical.

We note that Arzoumanian et al. (2019) do not correct the line densities of the filaments they analyse for the contribution from embedded cores, on the grounds that this contribution is small. It is worth noting that, even if this contribution is not small, it should not be discounted. Hydrostatic equilibrium only exists for an isothermal filament if the outward acceleration due to internal pressure, $\sim 4c_s^2/r$ balances the inward acceleration due to gravity, $\sim 2G\mu/r$. Any inward gravitational acceleration, be it due to relatively diffuse gas, dense cores or even protostars and stars, must be balanced for there to be an equilibrium. So μ should represent contributions from all sources of gravity inside the filament.

7.4 The Influence of S1 and HD147889 on Filament f1

As mentioned previously, the B stars S1 and HD147889 appear to influence the dense material in L1688. In particular, the section of f1 between the two stars has a much narrower width, and a much higher column density, than the rest of the filament, and coincides with a concentration of cores.

To quantify this, we define the straight line connecting S1 and HD147889 (the red line on Fig. 12) as the S1-HD147889 axis. On Fig. 17 we plot the surface density, Σ_0 , the mean dust temperature, \bar{T} , and the mean dust opacity index, $\bar{\beta}$, at each spine point, against its distance from the S1-HD147889 axis. The black filled circles represent spine points that lie on the south-east side of the S1-HD147889 axis, and the grey filled circles represent those that lie on the other side. The red outlined points correspond to local maxima in the column density.

Fig. 17a shows a strong peak in the surface density for spine points close to the S1-HD147889 axis, with a maximum of $\sim 680 M_\odot \text{pc}^{-2}$ actually on the axis. Σ_0 then decreases rapidly with distance from the S1-HD147889 axis, dropping by more than an order of magnitude over 0.2 pc on either side. Beyond this distance, Σ_0 is approximately constant at $300 \pm 100 M_\odot \text{pc}^{-2}$. There are well-defined local peaks at ~ 0.5 pc and ~ 0.8 pc from the S1-HD147889 axis, in both cases corresponding to features on the south-east side.

The column-density peak on the S1-HD147889 axis presumably reflects enhanced pressure from the regions surrounding S1 and/or HD147889 acting to compress the material within the filament. As shown on Fig. 12, this region has an exceptionally high density of cores, both near to, and along the filament spine. However, the width of the filament here is quite low, and – if one discounts the mass in cores – the line-density is actually less supercritical than many other filament sections in Ophiuchus. This suggests that compression by

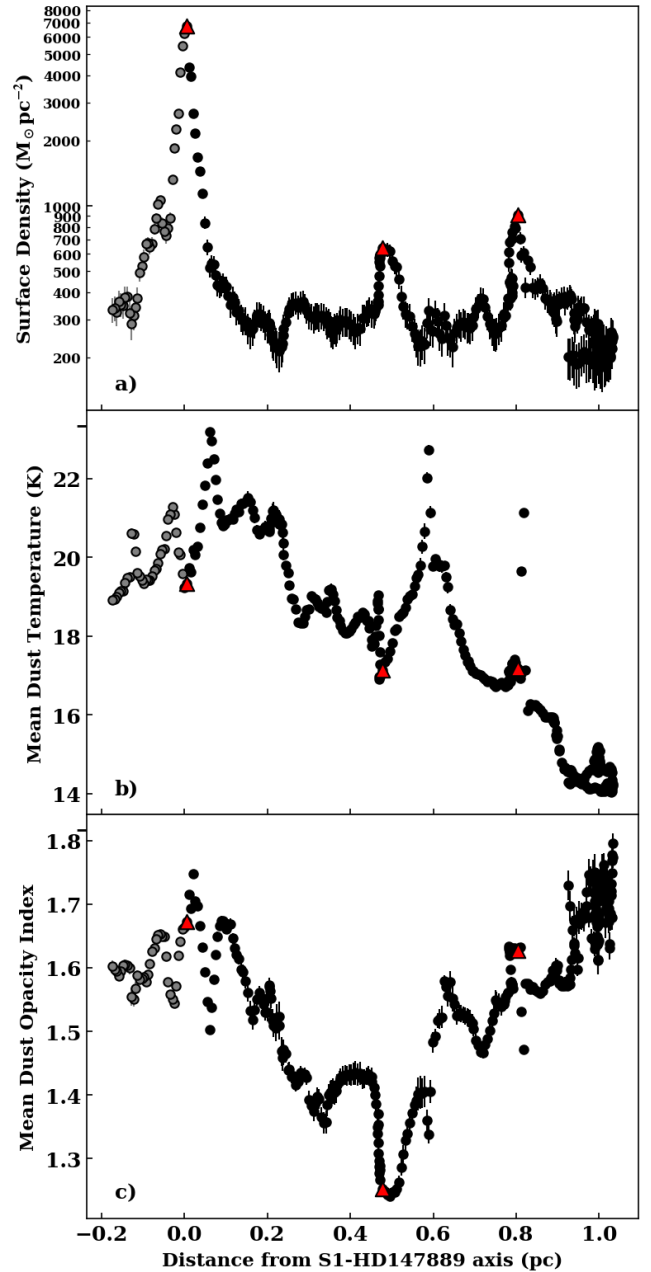


Figure 17. Plots of (a) surface density, Σ_0 , (b) mean dust temperature, \bar{T} , and (c) mean dust opacity index, $\bar{\beta}$, for the spine points of filament f1 in L1688, plotted against projected distance from the S1-HD147889 axis (see red line on Fig. 12). Grey-filled circles at negative value of the abscissa represent points north-west of this axis, and black-filled circles at positive value of the abscissa represent points to the south-east. Filled red triangles indicate the main local column-density maxima discussed in the text.

feedback from the nearby B stars may have induced efficient fragmentation. This scenario is further supported by the morphological features visible in the column-density and mean-temperature maps (Figs. 4 and 5a), which suggest compression waves emanating from the two B stars, especially S1.

Fig. 17b shows that the mean dust temperature on the spine points tends to fall with distance from the S1-HD147889 axis, implying that one or other of the PMS stars, and possibly both, are having a signifi-

cant heating effect on the filaments in their vicinity. Local peaks and troughs in the mean temperature presumably reflect locations where the dust in the filament is – respectively – exposed to additional radiation (for example, due to an embedded protostar) or more strongly shielded (for example, due to a dense but starless core). For example, at the spine points close to the S1-HD147889 axis, and at the spine points ~ 0.5 pc from the S1-HD147889 axis, column-density maxima coincide with minima in the mean dust temperature, but are closely flanked by maxima in the mean dust temperature, suggesting dense clumps or cores that have cold interiors but strongly externally heated envelopes.

There is no systematic correlation between the mean dust opacity index and distance from the S1-HD147889 axis on Fig. 17c, suggesting that the increased density and dust temperature in this region has not yet had any discernible influence on the mean physical or chemical properties of the dust. There is, however, a clear decrease in the dust opacity index at ~ 0.5 pc, coincident with the local column-density maximum there.

8 CONCLUSIONS

We have analysed *Herschel* and SCUBA-2 observations of the L1688 and L1689 sub-regions of the Ophiuchus molecular cloud, using the PPMAP algorithm. PPMAP returns a 4D data-hypercube giving, for each pixel on the sky, the surface density, Σ , as estimated from the opacity of dust of different types (represented by different opacity indices, β) and at different temperatures (T). Throughout both sub-regions, the PPMAP results show a network of filaments with complex temperature-coherent structures, and a systematic change in the dust properties in high-density regions, similar to that observed in the Taurus L1495 filament by Howard et al. (2019). We note the following features.

(i) The L1688 and L1689 sub-regions (defined, somewhat arbitrarily, by the black rectangles on Fig. 1) have average surface densities of $\sim 110 M_{\odot} \text{pc}^{-2}$ and $\sim 66 M_{\odot} \text{pc}^{-2}$ respectively.

(ii) $\sim 44\%$ of the mass in the L1688 sub-region is contained within High Efficiency Regions (HERs), defined as regions with $\Sigma \geq 160 M_{\odot} \text{pc}^{-2}$ (equivalent to $N_{\text{H}_2} \geq 7 \times 10^{21} \text{cm}^{-2}$, $A_{\text{V}} \geq 7$). HERs make up $\sim 22\%$ of the mass in the L1689 sub-region.

(iii) Taking the two sub-regions together, most starless and pre-stellar cores (300 out of 389) lie within the HERs, as already noted by Ladjelate et al. (2020).

(iv) Starless and prestellar cores account for 29% of the mass in the L1688 HERs, and 36% in the L1689 HERs.

(v) These results confirm the conclusion of Könyves et al. (2015) that there is a column-density threshold for efficient core formation, $\Sigma \geq 160 M_{\odot} \text{pc}^{-2}$ (equivalent to $N_{\text{H}_2} \geq 7 \times 10^{21} \text{cm}^{-2}$, $A_{\text{V}} \geq 7$); and they suggest that, once this threshold is exceeded, the core formation efficiency is approximately universal at $\eta \sim 0.5$, regardless of the wider environmental properties.

(vi) The filaments identified in L1688 all lie completely within HERs, while in L1689, two filaments fall entirely within HERs, one filament is partially located within an HER, and the final filament is found in the low density region bridging two HERs.

(vii) The filaments in L1688 are narrower, $\text{FWHM} = 0.11(\pm 0.04)$ pc, than those in L1689, $\text{FWHM} = 0.19(\pm 0.08)$ pc. However, after discounting the sections of filaments in L1689 that lie outside the HERs, the average filament width in L1689, $\text{FWHM} = 0.14(\pm 0.05)$ pc, is closer to those in L1688.

(viii) The mean line-density of the filaments in the two sub-regions are similar: $47(\pm 18) M_{\odot} \text{pc}^{-1}$ for L1688 and

$46(\pm 15) M_{\odot} \text{pc}^{-1}$ for L1689. If we adopt the canonical critical line density, $16.2 M_{\odot} \text{pc}^{-1}$, which presumes molecular gas at 10 K and ignores other forms of support (magnetic fields and/or turbulence), the filaments in both sub-regions are highly super-critical and should fragment rapidly.

(ix) On the basis of the Green Bank Ammonia Survey, Kerr et al. (2019) estimate that the dense cores in L1688 have a mean gas-kinetic temperature of ~ 18 K, and the somewhat less dense material in the filaments may be even warmer. If the gas-kinetic temperature in the filaments is 25 K, the critical line-density is $40.5 M_{\odot} \text{pc}^{-1}$. The filaments are then trans-critical, and fragmentation should be patchy. (Although the dust temperatures in the filaments are typically in the range ~ 17 K to ~ 24 K, the densities are probably too low for the gas and dust to be well coupled thermally.)

(x) Feedback from the B stars S1 and HD147889 appears to be compressing and heating a section of the f1 filament in L1688, where it passes between them, accelerating the rate of core formation there.

ACKNOWLEDGEMENTS

We thank the referee, Doris Arzoumanian, for her very thorough and thoughtful report, which helped us to improve the original version of this paper. This research made use of Photutils, an Astropy package for detection and photometry of astronomical sources (Bradley et al. 2016). ADPH gratefully acknowledges the support of a PhD studentship from the UK Science and Technology Facilities Council (STFC). APW, MJG and MWLS gratefully acknowledge the support of a Consolidated Grant (ST/K00926/1) from the STFC.

DATA AVAILABILITY

The observational data underpinning this article are collected from the *Herschel* Space Observatory and the James Clerk Maxwell Telescope (JCMT), and are publicly available from *Herschel* Science Archive (<http://archives.esac.esa.int/hsa/whsa>) and the JCMT Gould Belt Survey (<https://doi.org/10.11570/18.0005>), respectively. The core catalogue presented in Ladjelate et al. (2020) is publicly available from doi.org/10.26093/cds/vizier.36380074. The derived data generated in this research will be shared on request to the corresponding author.

REFERENCES

- André P., et al., 2010, *Astronomy & Astrophysics*, **518**, L102
 André P., Di Francesco J., Ward-Thompson D., Inutsuka S. I., Pudritz R. E., Pineda J. E., 2014, in Beuther H., Klessen R. S., Dullemond C. P., Henning T., eds, Protostars and Planets VI. p. 27 ([arXiv:1312.6232](https://arxiv.org/abs/1312.6232)), [doi:10.2458/azu_uapress_9780816531240-ch002](https://doi.org/10.2458/azu_uapress_9780816531240-ch002)
 Arzoumanian D., et al., 2011, *Astronomy & Astrophysics*, **529**, L6
 Arzoumanian D., et al., 2019, *Astronomy & Astrophysics*, **621**, A42
 Bernard J. P., et al., 2010, *Astronomy & Astrophysics*, **518**, L88
 Bradley L., et al., 2016, Astropy/Photutils: V0.3, Zenodo, [doi:10.5281/ZENODO.164986](https://doi.org/10.5281/ZENODO.164986)
 Chapin E. L., Berry D. S., Gibb A. G., Jenness T., Scott D., Tilanus R. P. J., Economou F., Holland W. S., 2013, *Monthly Notices of the Royal Astronomical Society*, **430**, 2545
 Exter K., 2017, *Herschel Explanatory Supplement*, III
 Greene T. P., Wilking B. A., André P., Young E. T., Lada C. J., 1994, *The Astrophysical Journal*, **434**, 614
 Griffin M. J., et al., 2010, *Astronomy & Astrophysics*, **518**, L3

- Hacar A., Tafalla M., Kauffmann J., Kovács A., 2013, *Astronomy & Astrophysics*, 554, A55
- Hildebrand R. H., 1983, *Quarterly Journal of the Royal Astronomical Society*, 24, 267
- Holland W. S., et al., 2013, *Monthly Notices of the Royal Astronomical Society*, 430, 2513
- Howard A. D. P., Whitworth A. P., Marsh K. A., Clarke S. D., Griffin M. J., Smith M. W. L., Lomax O. D., 2019, *Monthly Notices of the Royal Astronomical Society*, 489, 962
- Inutsuka S.-i., Miyama S. M., 1997, *The Astrophysical Journal*, 480, 681
- Kerr R., et al., 2019, *ApJ*, 874, 147
- Koch E. W., Rosolowsky E. W., 2015, *Monthly Notices of the Royal Astronomical Society*, 452, 3435
- Könyves V., et al., 2015, *Astronomy & Astrophysics*, 584, A91
- Lada C. J., Lombardi M., Alves J. F., 2010, *The Astrophysical Journal*, 724, 687
- Ladjele B., et al., 2020, *A&A*, 638, A74
- Loren R. B., 1989, *ApJ*, 338, 902
- Loren R. B., Wootten A., Wilking B. A., 1990, *ApJ*, 365, 269
- Lynds B. T., 1962, *The Astrophysical Journal Supplement Series*, 7, 1
- Mamajek E., 2008, *Astron. Nachr.*, 329, 10
- Marsh K. A., Whitworth A. P., Lomax O., 2015, *Monthly Notices of the Royal Astronomical Society*, 454, 4282
- Marsh K. A., et al., 2016, *Monthly Notices of the Royal Astronomical Society*, 459, 342
- Mundy L. G., Wootten A., Wilking B. A., Blake G. A., Sargent A. I., 1992, *The Astrophysical Journal*, 385, 306
- Nakamura F., Umemura M., 1999, *ApJ*, 515, 239
- Nutter D., Ward-Thompson D., André P., 2006, *Monthly Notices of the Royal Astronomical Society*, 368, 1833
- Ossenkopf V., Henning T., 1994, *Astronomy & Astrophysics*, 291, 943
- Ostriker J., 1964, *The Astrophysical Journal*, 140, 1056
- Padoan P., Nordlund Å., 2002, *ApJ*, 576, 870
- Palmeirim P., et al., 2013, *A&A*, 550, A38
- Pattle K., et al., 2015, *Monthly Notices of the Royal Astronomical Society*, 450, 1094
- Poglitsch A., et al., 2010, *Astronomy & Astrophysics*, 518, L2
- Schneider N., et al., 2012, *A&A*, 540, L11
- Shetty R., Kauffmann J., Schnee S., Goodman A. A., 2009a, *ApJ*, 696, 676
- Shetty R., Kauffmann J., Schnee S., Goodman A. A., Ercolano B., 2009b, *ApJ*, 696, 2234
- Soler J. D., 2019, *Astronomy & Astrophysics*, 629, A96
- Suri S., et al., 2019, *A&A*, 623, A142
- Valtchanov I., 2017, *Herschel Explanatory Supplement*, IV
- Vrba F. J., 1977, *AJ*, 82, 198
- Ward-Thompson D., et al., 2007, *The Publications of the Astronomical Society of the Pacific*, 119, 855
- Whitworth A. P., Ward-Thompson D., 2001, *ApJ*, 547, 317
- Whitworth A. P., et al., 2019, *MNRAS*, 489, 5436
- Wilking B. A., Lada C. J., 1983, *The Astrophysical Journal*, 274, 698

the L1688 sub-region, and 3.9 for the L1689 sub-region. The PPSD for the L1688 HER is 5.3, and 8.1 for the L1689 HER.

This paper has been typeset from a $\text{\TeX}/\text{\LaTeX}$ file prepared by the author.

APPENDIX A: POINT PROCESS STATISTICAL DEGENERACY

As discussed in Sec. 5, the PPSD (Eq. 13) gives a pixel-by-pixel measure of the statistical significance of the PPMAP optical-depth estimates, and hence also of the surface-density estimates. It is analogous to a signal-to-noise ratio, with $\text{PPSD} = 1$ indicating that the magnitude of an optical-depth estimate is equal to the magnitude of the uncertainty associated with that estimate, whereas $\text{PPSD} = 5$ indicates that the estimate is five times larger than the associated uncertainty, and so on.

Figs. A1a and A1b show the PPSD values for the L1688 and L1689 sub-regions of Ophiuchus. The mean PPSD value is 2.9 for

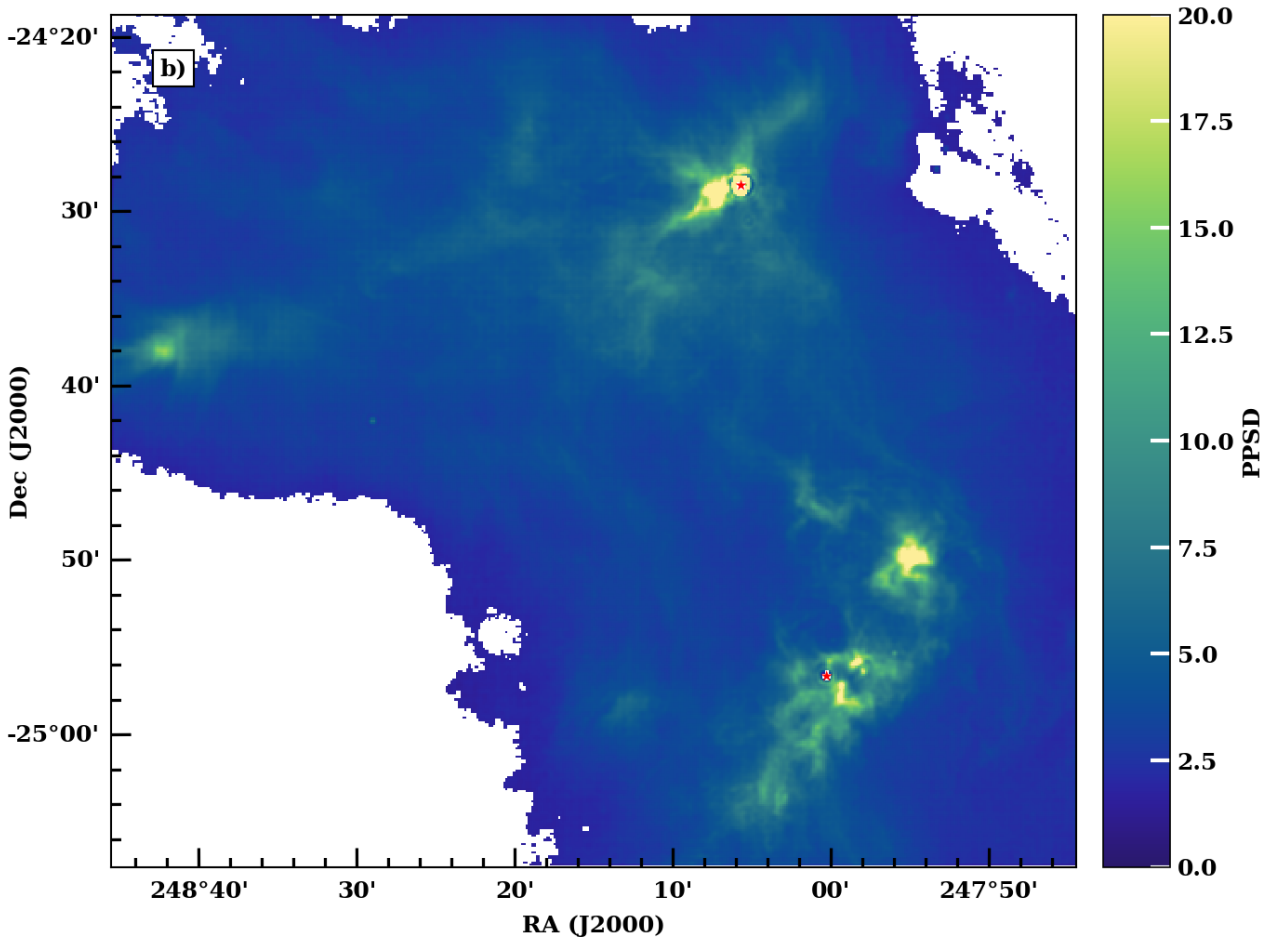
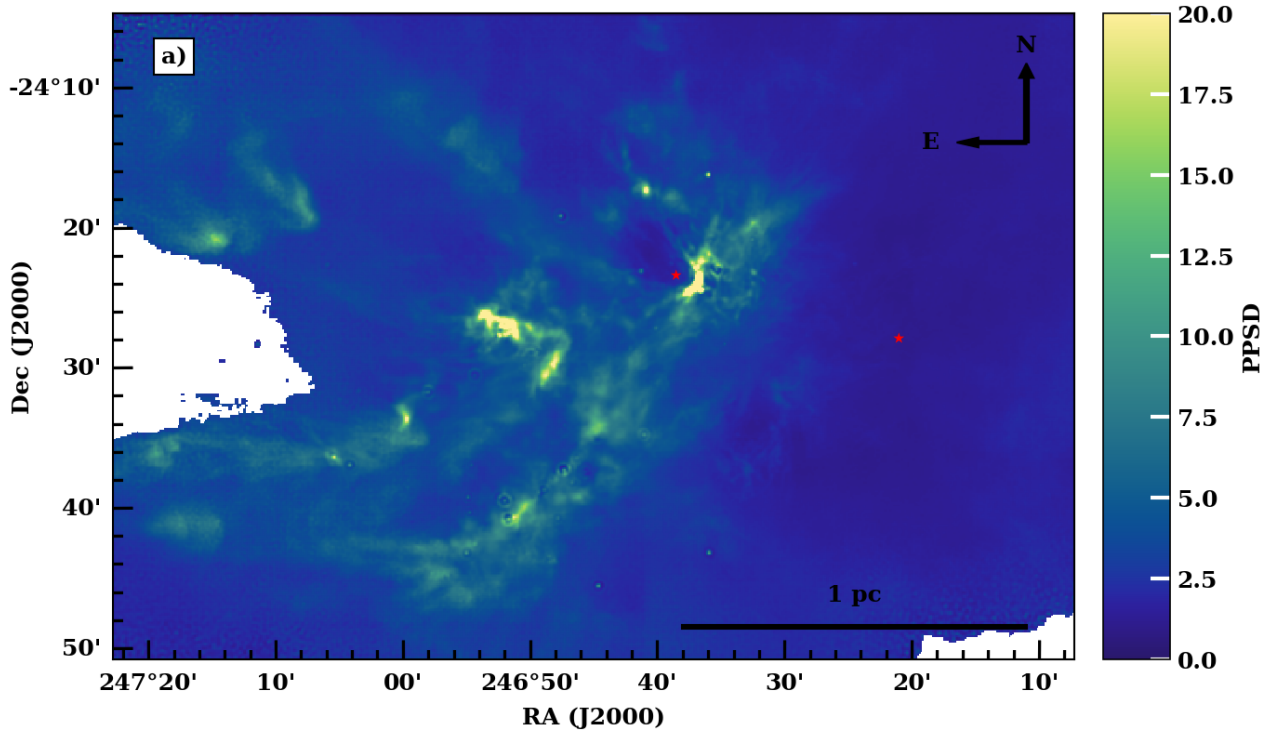


Figure A1. Pixel-by-pixel PPSD for (a) the L1688 sub-region, (b) the L1689 sub-region.